UNIVERSIDADEDE SÃO PAULO

INSTITUTO DE FÍSICA DE SÃO CARLOS

RAPHAELL JUNNIO MOREIRA SILVA

Structural characterization of fluorophosphate glasses using NMR methodologies

São Carlos
2014

RAPHAELL JUNNIO MOREIRA SILVA

Structural characterization of fluorophosphate glasses using NMR methodologies

Dissertation presented to the Graduate Program in Physics at the Instituto de Física de São Carlos, Universidade de São Paulo to obtain the degree of Master of Science.

Concentration area: Applied Physics
Option: Biomolecular Physics

Advisor: Prof. Dr. Hellmut Eckert.

Original Version

São Carlos
2014

Ficha catalográfica elaborada pelo Serviço de Biblioteca e Informação do IFSC,
com os dados fornecidos pelo(a) autor(a)

Moreira Silva, Raphaell Junnio
Structural characterization of fluorophosphate glasses using NMR methodologies / Raphaell Junnio Moreira Silva; orientador Hellmut Eckert -- São Carlos, 2014.
84 p.

Dissertação (Mestrado - Programa de Pós-Graduação em Física Aplicada Biomolecular) -- Instituto de Física de São Carlos, Universidade de São Paulo, 2014.

1. Nuclear Magnetic Resonance. 2. Fluorophosphate glasses. 3. Raman scattering of glass. I. Eckert, Hellmut, orient. II. Título.

FOLHA DE APROVAÇÃO

Raphaell Júnnio Moreira Silva

Dissertação apresentada ao Instituto de Física de São Carlos da Universidade de São Paulo para obtenção do título de Mestre em Ciências.
Área de Concentração: Física Aplicada – Opção: Física Biomolecular.

Aprovado(a) em: 09/06/2014

Comissão Julgadora

Prof(a). Dr(a). Hellmut Eckert

Instituição: IFSC/USP

Prof(a). Dr(a). José Fábian Schneider

Instituição: IFSC/USP

Prof(a). Dr(a). Ubirajara Pereira Rodrigues Filho

Instituição: IQSC/USP

ACKNOWLEDGEMENTS

I would like to thank my supervisor Prof. Dr. Hellmut Eckert for the opportunity to be a member of his group and also the scientific support.

Many thanks go to Julia Zimdars, Carsten Doerenkamp and Philipe Selter for kind and funny moments during my time in Münster.

I thank all my new friends in Sao Carlos and around the world during my Master, in special: Steffen Pelz, Victor Abranches, Christian Rivera, Daniel Jardon, Arthur Ferreira, Gisele Philippesen, Débora Corrêa, Bastian P., Eduardo Volnistem, Danielly Freire, Luciana Gomes, Thomas Brysch, Jinjun Ren, Melanie Siedow, Janie Thomas.

I kindly thank Andrea Staubermann for all the support with bureaucracy during my stay in Münster. I also thank Wilma Pröbsting for the thermal analysis and Jakob Kopp for his help relating to the NMR spectrometer.

For kind and funny moments in Berlin I thank Aaron Hanh and Sarah Kastner.

I would like thank the AK Eckert and LEMAF for all the help and scientific discussion, in special Frederik Berhrends.

I kindly thank Prof. Eduardo Azevêdo, Diogo de Oliveira, Tito Bonagamba for the scientific discussion, coffee and NMR!

I thank the Fundação de Amparo à Pesquisa do Estado de São Paulo (FAPESP) for the financial support during my Master.

I kindly thank my brothers: Paulo, Marilia, Mírian and Carlos for always believe in my ability.

I would like thank and dedicate this Master Thesis to my parents: Jose Moreira and Ivanilda Moreira.

“Learn from yesterday, live for today, hope for tomorrow. The important thing is not to stop questioning”

Albert Einstein

ABSTRACT

MOREIRA, R.J.S. **Structural characterization of fluorophosphate glasses using NMR methodologies** 2014. 84 p. Dissertation (Master in Science) - Instituto de Física de São Carlos, Universidade de São Paulo, São Carlos, 2014.

In this work was studied the development of structure/property correlations for new fluorophosphate glasses compositions: $[80Ba(PO_3)_2 - 20Al(PO_3)_3]_{1-x}[80BaF_2 - 20AlF_3]_x$($0 \leq \mathbf{x} \leq 40$ - mol%). Most suitable techniques for the structural analysis in case of disordered and amorphous material are Nuclear Magnetic Resonance (NMR) Spectroscopy and Raman scattering. Results from X-ray diffraction (XRD) and differential thermal analysis (DTA) reveal that amorphous samples were obtained for all glass compositions up to $\mathbf{x} \leq 30$. However, the fluorine quantification via ^{19}F MAS NMR suggests significant fluoride loss and/or fluoride/oxide replacement. Both ^{31}P and Raman results indicate gradual conversion of Q^2_m units to Q^1_m units with increasing the fluorine concentration. ^{19}F MAS NMR spectra indicate fluorine atoms in two different chemical environments bonded wither covalently to P-atoms or located in a mixed Al/Ba environment. The P-F assignment is confirmed by $^{19}F\{^{31}P\}$-REDOR experiments. ^{27}Al NMR spectra shows dominantly six-coordinated aluminium, and the $^{27}Al\{^{31}P\}$-REDOR data suggest nearly exclusive coordination of Al with phosphate species. The dipolar coupling constant obtained by $^{31}P\{^{31}P\}$-DRENAR are roughly consistent with ^{31}P spectral deconvolution suggesting the presence of $Q^1$and Q^2 species.

Keywords: Nuclear Magnetic Resonance.Fluorophosphate glasses. Raman scattering of glass

RESUMO

MOREIRA, R. J. S.**Caracterização estrutural de vidros fluorofosfatos utilizado metodologias de RMN.** 2014. 84 p. Dissertação (Mestrado em Ciências) - Instituto de Física de São Carlos, Universidade de São Paulo, São Carlos,2014.

O presente trabalho aborda o estudo de correlações entre estrutura e propriedade de uma nova composição de vidros fluorofosfato. O trabalho compreende na síntese e caracterização de vidros fluorofosfatos com a seguinte composição: $[80Ba(PO_3)_2 – 20Al(PO_3)_3]_{1-x}[80BaF_2 – 20AlF_3]_x$($0 \leq \mathbf{x} \leq 40$ - mol%).Ressonância Magnética Nuclear e Espalhamento Raman são técnicas indicadas no estudo estrutural de materiais amorfos, como por exemplo, os vidros. Através dos resultados obtidos por difração de raios-X (DRX) e análise térmica diferencial (DTA) confirmam a formação de um sólido amorfo com concentrações de íons fluoretos de até 30 mol%. No entanto, a partir dos resultados da quantificação dos íons fluoretos via ^{19}F RMN sugerem que houve uma quantidade significativa de perda de fluoreto ou ainda troca dos íons fluoretos por óxidos. Os espectros de ^{31}P e Raman indicam uma gradual conversão das unidades Q^2_m em Q^1_m com o aumento de x. ^{19}F RMN indica que os átomos de flúor estão em dois ambientes químicos distintos, onde os íons fluoretos estão ligados com átomos de fósforo ou distribuídos em um ambiente misto de Al/Ba. Resultados obtidos via $^{19}F\{^{31}P\}$-REDOR confirmam a formação da ligação P-F. Os espectros de ^{27}Al mostram a predominância dos átomos de alumínio com geometria octaédrica e ainda os resultados de $^{27}Al\{^{31}P\}$-REDOR sugerem uma coordenação preferencial dos Al com unidades fosfato. Através dos resultados dos acoplamentos dipolares homonucleares via $^{31}P\{^{31}P\}$-DRENAR corroboram com a deconvolução dos espectros de ^{31}P na atribuição das espécies Q^1_m e Q^2_m.

Palavras-chave: Ressonância Magnética Nuclear.Vidros fluorofosfato. Espalhamento Raman de vidro.

LIST OF FIGURES

Figure 1 - V-T diagram illustrating the relationships between the liquid, solid and glassy states. 21

Figure 2 - Schematic representation of Q^n phosphate tetrahedral units. 24

Figure 3- Orientation of the dipolar vectors between the nuclei I and S with respect to the magnetic field B_0. 32

Figure 4 - The magic angle orientation of 54.7° relative to the direction of the static field (B_0). 36

Figure 5 - Pulse sequence scheme and the coherence path using the z-filter. 37

Figure 6 - REDOR experiment shown for four rotor periods. (A) The reference signal is obtained by a rotor synchronized spin-echo experiment. (B) The dipolar interaction is re-introduced by π pulses on the non-observed I-channel. The time development of the heteronuclear dipolar Hamiltonian is also determined in both parts. 40

Figure 7 - Compensated REDOR pulse sequence. 43

Figure 8 - DRENAR pulse sequence based on re-coupling by POST-C7 blocks. 44

Figure 9 - Powder XRD data of the glass line $[80Ba(PO_3)_2 – 20Al(PO_3)_3]_{1-x}[80BaF_2 – 20AlF_3]_x$ ($0 \leq x \leq 40$ - mol%)examined in the present study. 51

Figure 10 - Representative DTA curve for the sample composition $[80Ba(PO_3)_2 – 20Al(PO_3)_3]_{75}[80BaF_2 – 20AlF_3]_{25}$. Exothermic events are represented by positive excursions. 52

Figure 11 - Raman spectra of $[80Ba(PO_3)_2 – 20Al(PO_3)_3]_{1-x}[80BaF_2 – 20AlF_3]_x$ ($0 \leq x \leq 30$ - mol%) glasses. 54

Figure 12 - Deconvolution of the single pulse ^{19}F NMR spectra in the fluorine quantification experiment for the samples x = 20 mol% using NaF (sharp peak at -221 ppm) (left) and 30 mol% using BaF_2 (sharp peak at -14.2 ppm) (right) as internal signal intensity reference compounds. 56

Figure 13 - ^{19}F MAS-NMR spectra of the glasses measured at 25 kHz. 57

Figure 14 - ^{19}F MAS NMR spectra with simulations where (-) denote P-bonded F species and (-) denote F species in a mixed Ca/Al environment. 58

Figure 15 - (A): $^{19}F\{^{31}P\}$-REDOR dephasing curve of glass containing 30 mol% (B):^{19}F line shapes for their glass in the absence (red curve) and the presence (black dashed curve) of dipolar dephasing for a fixed dipolar evolution time of 197 µs. 59

Figure 16 - ^{27}Al MAS NMR data measured at 14 kHz and 11.7 T. 60

Figure 17 - ^{27}Al MQ-MAS NMR spectrum of glass with the composition x = 30 measured at 11.7 T. 61

Figure 18 - $^{27}Al\{^{31}P\}$ REDOR dephasing curves of glasses with compositions x = 0 (top, right) and x = 30 (bottom, right) and ^{27}Al line shapes for the glasses with compositions x = 0 (top, left) and x = 30 (bottom, left) in the absence (red curve) and the presence (black curve) of dipolar recoupling for a fixed dipolar evolution time of 505 µs and 604 µs, respectively, indicating that the Al environment is affected by dipolar interactions with ^{31}P nuclei. 63

Figure 19 - ^{31}P MAS NMR spectra measured at a rotation frequency of 14 kHz. Spinning sidebands are indicated by asterisks. 64

Figure 20 - ^{31}P MAS NMR spectra with simulations of the x = 0 mol% (left) and x = 30 mol% (right)at 14.0 kHz. 65

Figure 21 - $^{31}P\{^{31}P\}$-DRENAR results for the glasses with compositions x = 0 (top) and x = 30 (bottom). Left parts show the dephasing curves and the corresponding parabolic approximations, while right parts show the corresponding^{31}PMAS-NMR spectra in the presence and absence of the dipolar recoupling at a dipolar mixing time of 570 µs. 67

LIST OF TABLES

Table 1 Properties of examined nuclei 48

Table 2 Glass compositions and thermal properties of the glass samples..... 53

Table3 Experimental results of the ^{19}F NMR quantification and peak deconvolution results 55

Table 4 Fitting parameters of the ^{19}F MAS NMR spectra at 4.70 T. δ is the chemical shift, *fwhm* is the full with at half maximum and A_{rel} is relative area.....58

Table 5 ^{27}Al chemical shifts and SOQE obtained from ^{27}Al MQ-MAS..... 62

Table 6 Second Moment Values $M_2(^{27}Al\{^{31}P\})$ obtained for the Al(VI) units* 63

Table7 ^{31}P MAS-NMR lineshape fitting parameters for $[80Ba(PO_3)_2 – 20Al(PO_3)_3]_{1-x}[80BaF_2 – 20AlF_3]_x$ ($0 \leq x \leq 30$) glasses 65

CONTENT

1 INTRODUCTION 19

2 BACKGROUND 21

2.1 The Vitreous State 21

2.2 Oxyfluoride and Fluorophosphate Glasses 23

2.3 Fundamental Aspects of NMR Spectroscopy 25

2.3.1 Internal Spin Interactions 27

2.3.2 Magnetic shielding 28

2.3.3 Quadrupolar interactions 29

2.3.4 Magnetic Dipole-Dipole Interactions 31

2.4 Methods of NMR Spectroscopy 34

2.4.1 Magic Angle Spinning – MAS 35

2.4.2 Multiple Quantum Magic Angle Spinning – MQMAS 36

2.4.4 Dipolar re-coupling effects nuclear alignment reduction - (DRENAR) 43

3 EXPERIMENTAL SECTION 47

3.1 Synthesis of the Glasses 47

3.2 Thermal Analysis 47

3.3 X-ray Diffraction 47

3.4 Raman Spectroscopy 48

3.5 Solid-State NMR Spectroscopy 48

3.5.1 Properties of the Examined Nuclei 48

3.5.2 Experimental Details of the NMR Measurements 49

3.5.4 MQ-MAS NMR Experiments 49

3.5.5 REDOR Experiments 50

3.5.6 DRENAR Experiments 50

4 RESULTS AND DISCUSSION 51

4.1 XRD Results 51

4.2 Thermal Analysis 52
4.3 Raman Scattering Results 53
4.4 NMR Results 54
4.3.1 Fluoride Quantification by ^{19}F NMR 54
4.3.2 Structural Characterization by ^{19}F MAS-NMR 56
4.3.3 $^{19}F\{^{31}P\}$-REDOR 59
4.3.4 Structural Characterization by ^{27}Al MAS- and MQMAS-NMR 60
4.3.5 $^{27}Al\{^{31}P\}$-REDOR 62
4.3.6 Structural Characterization by ^{31}P MAS-NMR 64
4.3.7 $^{31}P\{^{31}P\}$ – DRENAR 66
5 CONCLUSIONS AND PERSPECTIVES 69
REFERENCES 71
APPENDIX 77

1 INTRODUCTION

Glasses are immensely versatile materials and at the forefront in a multitude of high technology applications. These include optical devices, such as lasers, amplifiers, and biosensors. Regarding applications of glasses for laser development there is an ongoing search for new and efficient combinations of luminescent rare-earth ion or transition metal emitters with suitable crystalline, glassy or ceramic solid host materials. It is desired to decrease the sensitivity of such materials towards vibrational de-excitation and concentration quenching, while at the same time designing mechanically, thermally and chemically more robust materials that withstand mechanical stresses, adverse ambient environments, and elevated temperatures. In the search for such improved materials the development of structure/property correlations is essential for tailoring materials, composition and processing parameters to specific application demands and for exploring new avenues in research and development.

In this context, the present Master Thesis aims at the development of structure/property correlations for new fluorophosphate glass compositions. Most suitable techniques for the structural analysis of disordered and amorphous material are Nuclear Magnetic Resonance (NMR) Spectroscopy and Raman scattering. Fluorophosphate and Oxyfluoride glasses are of interest for laser applications, because they are known to offer favourable structural environments for rare earth (RE) ions, regarding their photophysical properties. Partial replacement of oxide by fluoride result in increased excited-state lifetimes and quantum yields relative to those properties obtained on than pure metaphosphate glasses.[1–4]By using ^{19}F-, ^{27}Al- and ^{31}P-NMR one- and two- dimensional experiments it will be possible to obtain complementary views on the atomic environments and gain new structural insights into the local coordination of the emitting rare-earth ions as well as of the amorphous frameworks that constitute their host environment. Up to now, only a few NMR studies of oxyfluoride and fluorophosphate glasses have been published, none of which are taking full advantage of the power and potential of advanced multidimensional solid state NMR spectroscopy. This deficiency will be remedied by the present study, the goal of which is to develop a comprehensive modern solid state NMR strategy towards the structural elucidation of fluorophosphates-based optical glasses.

2 BACKGROUND

2.1 The Vitreous State

The vitreous state combines the macroscopic characteristics of a solid with the structural disorder of a liquid. The mechanical properties are similar to those of the corresponding crystals, however, instead of a defined melting point glasses are characterized by a glass transition region .[5–7] Glass formation is basically a kinetic process that it is formed if the rate of cooling below the melting point of the substance is faster than the nucleation and crystallization rate.

From a physical-chemical point of view glass formation can be discussed based on the volume versus temperature diagram as shown in **Figure 1**.

Figure 1 – V-T diagram illustrating the relationships between the liquid, solid and glassy states.

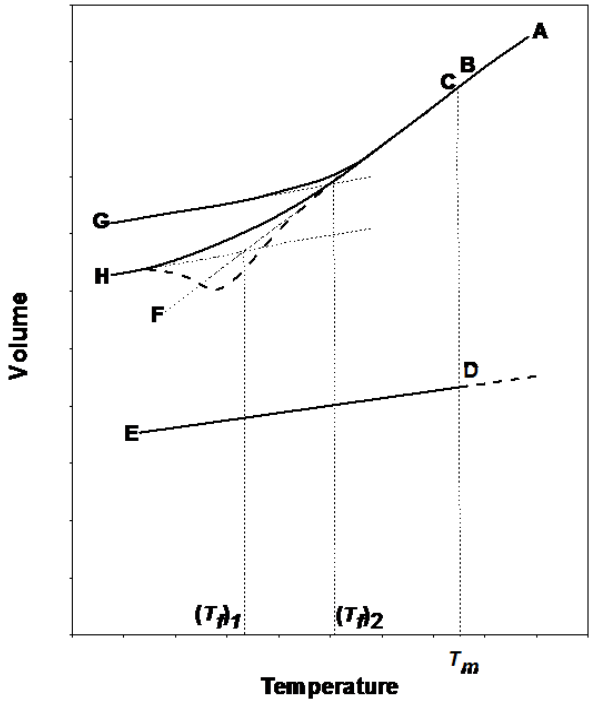

Source: Adapted from VARSHNEY[5]

At sufficiently high temperature the material is present in liquid form, represented by A. Along the cooling trajectory A-B-C the point B correspond to the crystallization temperature (or the melting temperature $T_m$of a crystal), the temperature at which the solid and liquid states have the identical same Gibbs energies (free enthalpies).[7-8]Below this temperature the crystalline state would be the

equilibrium state, however, the pre-requisite processes for establishing equilibrium nucleation and crystal growth are kinetic processes characterized by activation barriers. If the rates of these processes are slower than the cooling rates, crystallization can be suppressed, and the material remains in the metastable state of a supercooled liquid (trajectory B-C-F).[5] Concomitant with the cooling process, the viscosity of the liquid keeps increasing, further slowing down the transport mechanisms required for crystallization. Near the glass transition the liquid possesses a viscosity near 10^{12}-10^{13} Poise, at which point the timescale of molecular motion becomes comparable to the timescale of macroscopic experiments (1-1000 seconds).

In this temperature region the B-C-F trajectory becomes almost a straight parallel line to the corresponding trajectory of the crystal. The exact trajectory also depends on the cooling rates: if for fast cooling the D-E trajectory, ending at point G, is observed, the trajectory D-E-H is followed when the material is cooled more slowly. The glass transition region is characterized by rather abrupt changes in the thermal expansion coefficient α, the specific heat c_p, and the viscosity η. The glass transition temperature (T_g) can be determined from such measurements by looking for abrupt changes in the temperature coefficients of either α or η. Most frequently, T_g is measured by monitoring the abrupt increase in $c_p$via differential scanning calorimetric. This c_p increase is caused by the onset of atomic/molecular motion on the macroscopic timescale of bulk property measurements. Most commonly T_g is defined by the onset point of the heat capacity change associated with the glass transition. If the material is heated further above T_g, one can frequently observe crystallization exotherms (onset temperature T_x) in such measurements, signifying the re-establishment of thermodynamic equilibrium. The thermal stability of a glass is defined by the difference in the characteristic temperatures $\Delta T = T_x - T_g$. Kinetically very stable glasses are characterized by a large temperature difference or even the absence of crystallization processes during the linear heating conditions of thermal analysis experiments. Compositional trends in the glass transition temperatures and other macroscopic properties can be frequently related to the framework's bond connectivity (average coordination number) within the theoretical context of percolation theory.[9-10]

2.2 Oxyfluoride and Fluorophosphate Glasses

The favorable bulk characteristics of many oxide glasses, such as high mechanical strength and chemical stability and low refractive indices frequently conflict with unfavorable optical absorption and emission properties for the rare-earth dopant species. Likewise, the more favorable optical properties of fluoride glasses, such as high infrared transparency, long excited state lifetimes and high quantum yields due to inefficient vibrational de-excitation mechanisms come at the price of poor mechanical, chemical, and thermal stability. In this sense, oxyfluoride and fluorophosphate glasses not only present a compromise between these conflicting demands, but often can be designed to produce glasses that primarily combine the desirable properties of each glass family type, while avoiding the corresponding drawbacks. For example, fluorophosphate glasses have optical properties that are comparable to those of fluoride glasses and mechanical properties that are comparable to those of oxide glasses.[3,11] This favorable situation arises from the fact that the photophysical properties of the rare earth ion emitters are primarily controlled by the local environments of the rare earth ions (which are thought to be dominantly fluoride ions), whereas the bulk properties are dominated by the structural makeup of the host framework, which is strengthened by bridging oxygen atoms.[12–14]

Owing to this synergetic effect, fluorophosphate glasses have a variety of technological applications such as optical amplifiers and high power lasers.[15–17]Other applications benefit from unique combinations of mechanical and chemical properties. For example, lead tin fluorophosphate glasses have transition temperatures near 100°C, good chemical durability and can be used in low temperature moulding operations for optical devices, for example.[18]

For the design of compositions with improved physical properties, the development of structural concepts is essential. Owing to the lack of long-range order in these glasses, diffraction methods are fairly powerless, and the structural information is mostly extracted from spectroscopic measurements, such as Raman scattering[19–21] and NMR[22–27] spectroscopy. The short-range order of phosphate glasses is usually described in terms of the Q^n_mterminology: here*n* is the number of P next-nearest neighbors perP tetrahedron and *m* is the number of next-nearest neighbor atoms in those glasses that possess additional network forming species as

shown schematically in **Figure 2**

Figure 2 -Schematic representation of Q^n phosphate tetrahedral units.

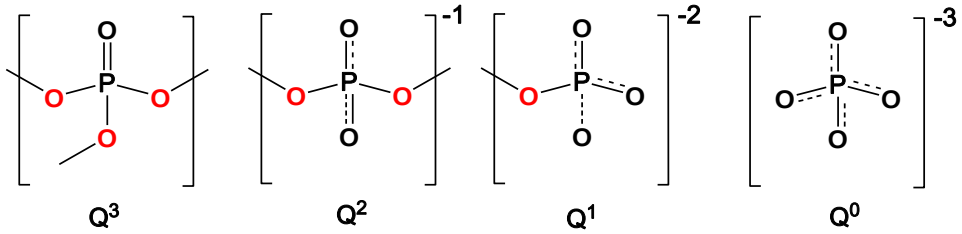

Source: By the Author

Addition of fluoride to metaphosphate glass is envisioned to result in network depolymerisation, the P-O-P bonds are broken to form mono- or difluorophosphate (PO_3F - Q^1-units or PO_2F_2 – Q^0-units).[28] Owing to this depolymerisation process, the average phosphate chain length is successively decreased, as increasing amounts of fluoride species are incorporated into the metaphosphate glass structure, this successive conversion finally leads to pyrophosphate dimmers. The process can be monitored by Raman spectroscopy where the appearance of anew scattering peak near 1020 cm^{-1} can be attributed to the symmetric stretching modes $\nu_s(PO_3^{2-})$ of the $Q^{(1)}$ units.[19,21] At the same time, the network-modifiers will form polyhedral arrangement, such as $Al(F,O)_6$, which was observed at 540 cm^{-1} and can act as a linker between the smaller phosphate chains (band at 540 cm^{-1}).[21]

NMR spectroscopy can give complementary insights about the short-range structure on the fluorophosphate glasses. For example, in the $30AlF_3$-$70NaPO_3$ system ^{27}Al MAS-NMR indicates the presence of octahedral Al-sites, the ^{19}F NMR spectra shows fluorine atoms interacting with both P and Al.[28-2931]P NMR results for this system shows Q^1-units coordinated with one or more Al.[28-29] A common issue in the preparation of fluorophosphate glasses is fluoride loss via evaporation, which can be quantified via ^{19}F NMR using a previously published method.[30]

2.3 Fundamental Aspects of NMR Spectroscopy

Nuclear Magnetic Resonance Spectroscopy (NMR) is based on the magnetic properties of atomic nuclei. This magnetism reflects their spin angular momentum, represented by the vector operator **I**, which does not have a classical analogue.[31-32] As proven by Stern-Gerlach experiments, nuclear spins are subject to orientational quantization, according to $\mu_z = m\hbar$, with energetically degenerate characterized by the quantum number $m \in \{I, I-1, I-2 \ldots -I\}$, where **I** is the nuclear spin quantum number. Each nuclear magnetic moment (μ) is related to the nuclear spin***I*** of the nucleus is given by [33–35]

$$\vec{\boldsymbol{\mu}} = \boldsymbol{\gamma}\hbar\vec{\mathbf{I}} \qquad \textbf{(1)}$$

Hereγ is the magnetogyric ratio, characteristic for each type of nucleus with dimensions $T^{-1}s^{-1}$and $\hbar$ is $h/2\pi$ (h = Planck's constant). In the presence of an external magnetic field B_0, the magnetic moment interacts with this field, with the interaction energy equal to

$$\mathbf{E} = -\vec{\boldsymbol{\mu}} \cdot \overrightarrow{\mathbf{B_0}} \qquad \textbf{(2)}$$

Considering the static magnetic field oriented along the z-direction, the interaction energy is given by

$$\mathbf{E} = -\boldsymbol{\gamma}\,\hbar\,|\vec{\mathbf{I}}_\mathbf{z}|\mathbf{B_0} \qquad \textbf{(3)}$$

In the presence of the external field the nuclear spin orientational states loose degeneracy owing to the Zeeman interaction resulting in discrete energy levels.

$$\mathbf{E_{ml}} = -\mathbf{m_l}\,\boldsymbol{\gamma}\,\hbar\,\mathbf{B_0} \qquad \textbf{(4)}$$

Transitions between adjacent states (selection rule $\Delta m = \pm 1$) can be stimulated through the fluctuating magnetic fields associated with electromagnetic waves of

suitable energy.[33] In the case of resonance the energy level difference between adjacent Zeeman states

$$\Delta \mathbf{E} = \hbar \boldsymbol{\gamma}\, \mathbf{B_0} \tag{5}$$

is equal to the energy of the electromagnetic radiation absorbed to induce these transitions. The resonance frequency thus defined via ΔE/h is also identical to the frequency of nuclear precession (Larmor frequency$\boldsymbol{\omega_L}$)[33-34]

$$\boldsymbol{\omega_L} = {}^{\mathbf{\Delta E}}\!/_{\mathbf{h}} = {}^{\boldsymbol{\gamma}\, \mathbf{B_{loc}}}\!/_{\mathbf{2\,\pi}} \tag{6}$$

where $B_{loc} = B_0 + B_{int}$is the local field experienced by the nuclei and comprises the sum of the externally applied and the internal fields.

At thermal equilibrium, a macroscopic sample develops a magnetization parallel to the externally applied magnetic field (z-direction) as a consequence of the Boltzmann distribution. The applied radio frequency (r.f), oscillating with the frequency $\omega_o \sim \omega_L$produces transitions between the Zeeman levels and imparts a time dependence on the magnetization vector. The trajectory of the magnetization is best described by a vector model in a coordinate frame rotating with the frequency ω_0 around the z direction.

The Zeeman interaction between the oscillating magnetic field, $B_1(t)$, and the nuclear spins is described by the Hamiltonian[33]

$$\widehat{\mathbf{H}}_{\mathbf{rf}} = -\boldsymbol{\gamma_1} \hbar\, \mathbf{2\, B_1} \hat{\mathbf{I}}_{\mathbf{x}} \cos \boldsymbol{\omega_0} \mathbf{t} \tag{7}$$

where $B_1(t) = 2\, B_1 \cos \omega_0 t$.

In the classical vector model the magnetization is described in the laboratory coordinate system (x, y, z) by a gyratory movement around the static field vector $\mathbf{B_0}$, and the oscillating $\mathbf{B_1}$, vector associated with the electromagnetic waves.(36–38) The description of the effect of the B_1 field can be simplified in a coordinate system (x', y', z') which rotates with the frequency of the field $\omega_0$about the z-axis. In this *rotating*

coordinate system the B_1direction can be described as fixed along the x'-axis and the magnetization precesses about this axis, following a circular trajectory in the zy plane. Applying the B_1 field for a short duration (pulse length) $t_p$to the magnetization vector inclines its orientation relative to the z axis by an angle α.[33]

$$\boldsymbol{\alpha = \gamma\, t_p\, |\vec{B}_1|} \tag{8}$$

For NMR signal detection, usually a 90° pulse is applied. Subsequent to this pulse, the transverse magnetization thus generated precesses with the Larmor frequency in the x-y plane under the influence the static magnetic field B_0.[33,37]This precessingmagnetization produces a flux change within a stationary coil oriented perpendicular to the magnetic field direction, resulting in an induced oscillating voltage, which constitutes the NMR signal. Its amplitude decays in time owing to relaxation processes.[37] The NMR signal is acquired in the time domain f(t), digitized and converted to a frequency domain signal via Fourier Transformation[36]

$$\boldsymbol{F(\omega) = \int_{-\infty}^{\infty} f(t) e^{-i\omega t} dt} \tag{9}$$

2.3.1 Internal Spin Interactions

The Larmor frequencies in standard NMR experiments are generally dominated by Zeeman interactions. However, the precise precession frequencies are also influenced by a number of internal interactions which reflect details about the local structural environment. Their influence upon the Zeeman energy levels can be calculated using perturbation theory.

The total spin Hamiltonian can be represented by[23,39–41]

$$\boldsymbol{\hat{H}_{total} = \hat{H}_z + \hat{H}_{rf} + \hat{H}_{ms} + \hat{H}_d + \hat{H}_J + \hat{H}_Q} \tag{10}$$

Here, $\hat{\mathbf{H}}_{\mathbf{ms}} + \hat{\mathbf{H}}_{\mathbf{b}} + \hat{\mathbf{H}}_{\mathbf{J}} + \hat{\mathbf{H}}_{\mathbf{Q}}$describe distinct internal interactions, such as: (1) magnetic shielding, (2) dipole-dipole coupling (direct and indirect) and (3) nuclear electric quadrupolar interactions. The last term, which describes the interaction of the nuclear electric quadrupole moments and electrostatic field gradients at the nuclear origin, only occurs for nuclear spins with I> ½. [33]

2.3.2 Magnetic shielding

The applied external magnetic field induces currents in the electron shells causing additional magnetic fields with components either along or opposed to the B_0 direction.[33] The effective magnetic field experienced by the nuclei is a sum of the external magnetic field and all the induced magnetic field components.

In general the magnetic shielding is an anisotropic quantity and thus depends on the orientation of the molecule with respect to the external magnetic field. This property is expressed by the magnetic shielding tensor ($\overleftrightarrow{\boldsymbol{\sigma}}$) modifying the Zeeman interaction according to[34]

$$\hat{\mathbf{H}}_{\mathbf{MS}} = \boldsymbol{\gamma}\, \hat{\mathbf{I}} \overleftrightarrow{\boldsymbol{\sigma}} \mathbf{B_0} \tag{11}$$

With

$$\underset{\boldsymbol{\sigma}}{\leftrightarrow} = \begin{pmatrix} \boldsymbol{\sigma}_{\mathbf{xx}} & \boldsymbol{\sigma}_{\mathbf{xy}} & \boldsymbol{\sigma}_{\mathbf{xz}} \\ \boldsymbol{\sigma}_{\mathbf{yx}} & \boldsymbol{\sigma}_{\mathbf{yy}} & \boldsymbol{\sigma}_{\mathbf{yz}} \\ \boldsymbol{\sigma}_{\mathbf{zx}} & \boldsymbol{\sigma}_{\mathbf{zy}} & \boldsymbol{\sigma}_{\mathbf{zz}} \end{pmatrix} \tag{12}$$

The magnetic shielding tensor adopts a diagonal form in the Principal Axis System (PAS) with the components $\boldsymbol{\sigma}_{\mathbf{ii}}^{\mathbf{PAS}}$(I = x, y z), following the definition[34]

$$\left|\boldsymbol{\sigma}_{\mathbf{yy}}^{\mathbf{PAS}} - \boldsymbol{\sigma}_{\mathbf{iso}}^{\mathbf{PAS}}\right| \leq \left|\boldsymbol{\sigma}_{\mathbf{xx}}^{\mathbf{PAS}} - \boldsymbol{\sigma}_{\mathbf{iso}}^{\mathbf{PAS}}\right| \leq \left|\boldsymbol{\sigma}_{\mathbf{zz}}^{\mathbf{PAS}} - \boldsymbol{\sigma}_{\mathbf{iso}}^{\mathbf{PAS}}\right| \tag{13}$$

Linear combinations of these principal axis components are often used to describe the isotropic(σ_{iso}), anisotropic ($\Delta\sigma$)and asymmetric components (η) defined according to[42]

$$\boldsymbol{\sigma_{iso} = \frac{1}{3}\left(\sigma_{zz}^{PAS} + \sigma_{yy}^{PAS} + \sigma_{xx}^{PAS}\right)}$$

$$\boldsymbol{\Delta\sigma = \sigma_{zz}^{PAS} - \frac{1}{2}\left(\sigma_{yy}^{PAS} + \sigma_{xx}^{PAS}\right)} \qquad \textbf{(14)}$$

$$\boldsymbol{\eta = \frac{\sigma_{xx}^{PAS} - \sigma_{yy}^{PAS}}{\sigma_{zz} - \sigma_{iso}}}$$

The nuclear precession frequency (ω_L) for any orientationθ and ϕ can be obtained by[42]

$$\boldsymbol{\omega_L = -\omega_n\left\{1 - \sigma_{iso} + \frac{1}{2}\Delta\left[(3\cos^2\theta - 1) + \eta\sin^2\theta\cos 2\phi\right]\right\}} \qquad \textbf{(15)}$$

whereω_n is the nuclear Larmorfrequency in the absence of shielding effects (bare nucleus) and θ andϕ define the orientation of the PAS in the laboratory frame.[42] As absolute shielding values are experimentally inaccessible (bare nuclei are non-existent) the frequencies of the sample under investigation are referenced to those of a standard substance. In this fashion a *chemical shifts*is defined according to[34]

$$\boldsymbol{\delta_{cs} = \frac{\omega_L - \omega_{ref}}{\omega_{ref}}} \qquad \textbf{(16)}$$

2.3.3 Quadrupolar interactions

Nuclei with spin quantum number ***I***> ½ are characterized by an asymmetric charge distribution described by a nuclear electric quadrupole moment.[33] Such nuclei interact with electric field gradients, generated by the surrounding charge distribution (electron shell).[33] The Hamiltonian for the spin ***I*** describing this interaction in spin coordinates is given by [33]

$$\widehat{\mathbf{H_Q}} = \frac{\mathbf{e\,Q}}{\mathbf{2\,I\,(I+1)}\hbar}\hat{\mathbf{I}}\overleftrightarrow{\mathbf{V}}\hat{\mathbf{I}} \qquad \textbf{(17)}$$

Here Q is the nuclear electric quadrupole moment and ($\overleftrightarrow{\mathbf{V}}$) is the electric field gradient tensor. **Equation 17** can be re-written as [42]

$$\widehat{\mathbf{H}}_\mathbf{Q} = \frac{\mathbf{e\,Q}}{\mathbf{6\,I\,(2I-1)}\hbar}\sum_{\boldsymbol{\alpha,\beta=x,y,z}} \mathbf{V_{\alpha\beta}}\left[\mathbf{3/2}\left(\widehat{\mathbf{I_\alpha}}\,\widehat{\mathbf{I_\beta}} + \widehat{\mathbf{I_\beta}}\,\widehat{\mathbf{I_\alpha}}\right) - \boldsymbol{\delta_{\alpha\beta}}\widehat{\mathbf{I^2}}\right] \qquad \textbf{(18)}$$

whereα, β refer to x, y, z of whatever frame of reference the spin operators and the electric gradient field tensor are defined. Since $\sum \mathbf{V_{ii}} = \mathbf{0}$(Laplace Equation) the description of the electric field gradient tensor in the principal axis system is reduced to only two parameters defined by [42]

$$\mathbf{eq} = \mathbf{V_{zz}^{PAS}}$$
$$\boldsymbol{\eta}_\mathbf{Q} = \frac{\mathbf{V_{xx}^{PAS}} - \mathbf{V_{yy}^{PAS}}}{\mathbf{V_{zz}^{PAS}}} \qquad \textbf{(19)}$$

Here $V_{zz}^{PAS}$is the maximal value measured along the direction of the principal axis and $\eta_Q$describes the deviation of the electric field gradient from axial (cylindrical) symmetry. In terms of these parameters, the quadrupolar Hamiltonian can be re-written as [42]

$$\widehat{\mathbf{H_Q}} = \frac{\mathbf{e^2\,q\,Q}}{\mathbf{4\,I\,(2\,I-1)}\hbar}\left[\mathbf{3}\,\hat{\mathbf{I}}^\mathbf{2}_\mathbf{z\,PAS} - \hat{\mathbf{I}}^\mathbf{2} + \frac{\mathbf{1}}{\mathbf{2}}\boldsymbol{\eta}_\mathbf{Q}\left(\hat{\mathbf{I}}^\mathbf{2}_\mathbf{x\,PAS} - \hat{\mathbf{I}}^\mathbf{2}_\mathbf{y\,PAS}\right)\right] \qquad \textbf{(20)}$$

with.

$$\mathbf{C_Q} = \frac{\mathbf{e^2 Vzz\,Q}}{\hbar} \qquad \textbf{(21)}$$

defined as the nuclear electric quadrupolar coupling constant.[33]

When the quadrupolar interaction is weak compared with the Zeeman interaction the nuclear spin can still be considered quantized in the externally applied

magnetic field and the influence of the quadrupolar interaction upon the NMR spectra can be described by first order perturbation theory. The Hamiltonian can be expressed in this condition as [33]

$$\widehat{\mathbf{H_Q}} = \frac{\mathbf{C_Q}}{\mathbf{8\,I\,(2\,I-1)}}\left[\mathbf{3\cos^2\beta - 1 + \eta\sin^2\beta\cos(2\gamma)\{3\hat{I}_z^2 - \hat{I}(\hat{I}+1)\}}\right] \quad \textbf{(22)}$$

Here, the Euler angles relating the principal axis system to the laboratory coordinate system are represented by β andγ. The first order perturbation integral $\langle m|H_Q|\, m\rangle$must be evaluated and added as a correction term to the Zeeman eigenvalues for each m-state. Since to first order the energy arising from the quadrupolar interaction is a function of m² rather than m, the central transition energy $|\,{}^1/_2> \leftrightarrow |-{}^1/_2>$ is not altered and hence not subject to any anisotropy.[33]

For stronger quadrupolar coupling ($C_Q \geq 1$ MHz) at typical field strengths of 11.7 T), the perturbation treatment has to be extended to second order.[34] The perturbation is no longer field independent and causes shifts and anisotropic broadening effects also for the central transition lineshapes. The anisotropically broadened powder patterns depend on the value of the asymmetry parameter η_Q in a characteristic fashion, and η_Q can be determined from the latter with the help of simulations.[33-34]

2.3.4 Magnetic Dipole-Dipole Interactions

The third type of nuclear spin interactions that may affect NMR lineshapes in solids are the magnetic dipole-dipole interactions.[33-34] Generally two physically distinct contributions can be discriminated: (i) direct dipole-dipole couplings, which act through space and (ii) indirect dipole-dipole couplings (also called scalar or J-couplings) which are communicated via the polarization of electrons forming sequences of one to four chemical bonds between the nuclei under consideration.[33] While the tensor describing the direct dipole-dipole interaction is traceless, the J-tensor always contains an isotropic component which is independent of molecular orientation.

Figure 3 illustrates the orientational dependence of the dipolar interaction between two magnetic moments μ_s and μ_I.

Figure 3- Orientation of the dipolar vectors between the nuclei I and S with respect to the magnetic field B_0.

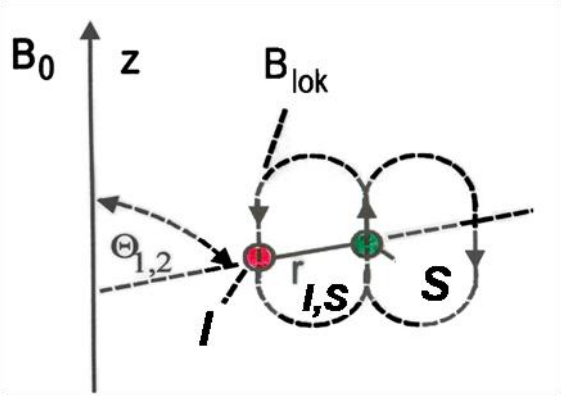

Source: Adapted from ECKERT.[43]

As illustrated in **Figure 3**, an S-spin is closeto the I-spin will experience a local field generated by the magnetic moment of the latter and vice-versa. For a two spin system the resulting interaction energy is described by [43]

$$\mathbf{E_{dip}^{IS}} = \frac{\mu_I . \mu_S}{\mathbf{r_{IS}^3}} - 3\frac{(\mu_I . \mathbf{r_{IS}})(\mu_S . \mathbf{r_{IS}})}{\mathbf{r_{IS}^5}} \quad \textbf{(23)}$$

Wherer_{IS} is the internuclear distance vector. Transforming the description of this vector into the polar coordinate system, and expanding the magnetic moments in terms of the individual spin coordinates leads to[34]

$$\widehat{\mathbf{H_D}} = \mathbf{d}\left[\hat{\mathbf{A}} + \hat{\mathbf{B}} + \hat{\mathbf{C}} + \hat{\mathbf{D}} + \hat{\mathbf{E}} + \hat{\mathbf{F}}\right] \quad \textbf{(24)}$$

where:

$$\mathbf{d} = \frac{\mu_0}{4\pi}\frac{\gamma_I \gamma_S \hbar}{r_{IS}^3}$$

$$\hat{A} = (3\cos^2\theta - 1)\hat{I}_z\hat{S}_z$$

$$\hat{B} = -\frac{1}{4}\left[\hat{I}_+\hat{S}_- + \hat{I}_-\hat{S}_+\right](3\cos^2\theta - 1)$$

$$\hat{C} = \frac{3}{2}\left[\hat{I}_z\hat{S}_+ + \hat{I}_+\hat{S}_z\right]\text{sen}\theta\cos\theta e^{-i\varphi} \qquad (25)$$

$$\hat{D} = \frac{3}{2}\left[\hat{I}_z\hat{S}_- + \hat{I}_-\hat{S}_z\right]\text{sen}\theta\cos\theta e^{+i\varphi}$$

$$\hat{E} = \frac{3}{4}\left[\hat{I}_+\hat{S}_+\right]\text{sen}^2\theta e^{-2i\varphi}$$

$$\hat{F} = \frac{3}{4}\left[\hat{I}_-\hat{S}_-\right]\text{sen}^2\theta e^{+2i\varphi}$$

The operators $\widehat{I_+}$ and $\widehat{S_+}$ and $\widehat{I_-}$ and $\widehat{S_-}$ are the raising and the lowering operators, respectively, and Θ is the angle between the external magnetic field and the internuclear vector r_{IS}.

In the limit of first order perturbation theory the description by the terms A and B is sufficient in the homonuclear case while the terms C to F vanish, resulting in a truncated Hamiltonian ("Secular Hamiltonian").[34] In the heteronuclear case, the truncated Hamiltonian comprises term A exclusively.[34]

$$\hat{H}_D^{homo} = -\frac{1}{2}\,\mathbf{d}\,(3\cos^2\theta - 1)[3\hat{I}_z^i\hat{I}_z^s - \mathbf{I}^i\mathbf{I}^j] \qquad (26)$$

$$\hat{H}_D^{hetero} = \mathbf{d}\,(3\cos^2\theta - 1)\hat{I}_z\hat{S}_z \qquad (27)$$

For the description of multi-spin systems it is convenient to use an expansion technique described by van Vleck.[40,44] The expansion is in terms of the moments M_n of the NMR lineshapes. The nth moment of f(ω) is defined by

$$\langle \mathbf{M^n} \rangle = \frac{\int_{-\infty}^{\infty} (\boldsymbol{\omega} - \langle \boldsymbol{\omega} \rangle)^{\mathbf{n}} \, \mathbf{f}(\boldsymbol{\omega}) \mathbf{d}\boldsymbol{\omega}}{\int_{-\infty}^{\infty} \mathbf{f}(\boldsymbol{\omega}) \mathbf{d}\boldsymbol{\omega}} \tag{28}$$

For n = 2 the so-called *second moment*has special significance, as it is directly calculable from internuclear distance distributions without knowing the precise spin geometries [34]

$$\mathbf{M_2^{homo}} = \frac{\mathbf{3}}{\mathbf{4}} \left(\frac{\mu_0}{\mathbf{4\pi}} \right)^{\mathbf{2}} \boldsymbol{\gamma}^{\mathbf{4}} \hbar^{\mathbf{2}} \mathbf{I} \, (\mathbf{I} + \mathbf{1}) \sum_{\mathbf{I} \neq \mathbf{S}} \frac{\left(\mathbf{1} - \mathbf{3cos^2 \theta_{ij}} \right)^{\mathbf{2}}}{\mathbf{r_{IS}^6}} \tag{29}$$

In case of heteronuclear M_2 only the A term from the dipolar alphabet is considered leading to the expression [34]

$$\mathbf{M_2^{hetero}} = \frac{\mathbf{1}}{\mathbf{3}} \left(\frac{\mu_0}{\mathbf{4\pi}} \right)^{\mathbf{2}} \boldsymbol{\gamma}_{\mathbf{I}}^{\mathbf{2}} \boldsymbol{\gamma}_{\mathbf{S}}^{\mathbf{2}} \hbar^{\mathbf{2}} \mathbf{S} \, (\mathbf{S} + \mathbf{1}) \sum_{\mathbf{S}} \frac{(\mathbf{1} - \mathbf{3cos^2 \theta_{IS}})^{\mathbf{2}}}{\mathbf{r_{IS}^6}} \tag{30}$$

For amorphous compounds or polycrystalline powders with statistically distributed orientations of the internuclear vectors relative to $B_o$the average value $\overline{(\mathbf{1} - \mathbf{3cos^2 \theta_{IS}})^{\mathbf{2}}} = {}^{\mathbf{4}}/_{\mathbf{5}}$ can be substituted, leading to [34]

$$\begin{aligned} \mathbf{M_2^{homo}} &= \frac{\mathbf{3}}{\mathbf{5}} \left(\frac{\mu_0}{\mathbf{4\pi}} \right)^{\mathbf{2}} \boldsymbol{\gamma}^{\mathbf{4}} \hbar^{\mathbf{2}} \mathbf{I} \, (\mathbf{I} + \mathbf{1}) \sum_{\mathbf{I} \neq \mathbf{S}} \mathbf{r_{ij}^{-6}} \\ \mathbf{M_2^{hetero}} &= \frac{\mathbf{4}}{\mathbf{15}} \left(\frac{\mu_0}{\mathbf{4\pi}} \right)^{\mathbf{2}} \boldsymbol{\gamma}_{\mathbf{I}}^{\mathbf{2}} \boldsymbol{\gamma}_{\mathbf{S}}^{\mathbf{2}} \hbar^{\mathbf{2}} \mathbf{S} \, (\mathbf{S} + \mathbf{1}) \sum_{\mathbf{S}} \mathbf{r_{IS}^{-6}} \end{aligned} \tag{31}$$

2.4 Methods of NMR Spectroscopy

Materials important in glass science present a much bigger challenge to structure elucidation than crystalline materials. In thehe absence of a a lattice with

translational symmetry no coherent x-ray diffraction can occur, making this method rather powerless for structural analysis.It is usually convenient to discuss the structural organization of glasses in separate terms on different length scales: (i) short range order, comprising the immediate local atomic environments of the atoms considered, (ii) medium-range order, involving the connectivity between the constituents of the glass matrix, the spatialcorrelations between network formers and network modifiers, as well as the modifier distribution in space. At larger distance scales, atomic segregation effects and details of the nucleation and crystal growth processes are of interest. NMR remains the most powerful spectroscopic approach for the study of structural issues on the 0.3 – 3 nm length scale.[43] Among the many types of internal interactions affecting NMR spectra the direct dipole-dipole interactions provide structural information (namely average internuclear distances and their distributions) in the most straightforward manner.[34,43] However, one difficulty arises from the fact that the spins are influenced by multiple internal interactions. For this reason it is important to employ *selective averaging* techniques, by means of which the Hamiltonian can be simplified such that only one (or few) type(s) of interaction(s) dominate(s). In the following section the most commonly employed methods will be introduced and shown “at work” in the structural analysis of glasses.

2.4.1 Magic Angle Spinning – MAS

Owing to the above-described anisotropic broadening mechanisms, NMR spectra of solid samples NMR are often subject to excessive broadening effects.

The fast isotropic Brownian motion that occurs in low-viscosity liquid media is sufficiently fast relative to the NMR time scale and thus results in complete orientational averaging, leading to highly resolved spectra with narrow lines. [34]By using the *magic-angle spinning* approach it is possible achieve the same results for solids.[45-46]**Equations 16**, **22** and **25** reveal that the magnetic shielding, the dipole-dipole interaction, and the first-order quadrupolar interactions have the same orientational dependence, namely $\mathbf{3cos^2\theta - 1}$. All of these anisotropic contributions can be eliminated by spinning a sample at high speed about an axis inclined at the magic angle of 54.7° (zero point of the 2nd Legendre polynomial) relative to the applied magnetic field direction. (see**Figure 4**.)

Figure 4 - The magic angle orientation of 54.7° relative to the direction of the static field (B_0).

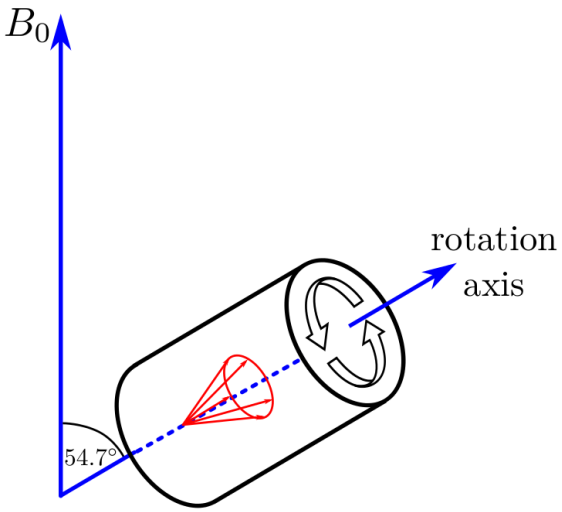

Source: Adapted from DUER. [34]

In two cases it is not possible to get high resolution NMR spectra, with narrow lines by using MAS: (1) whenever second-order quadrupolar perturbations are present, producing more a complicated orientational dependence, and (2) when the NMR resonance frequency is defined by a distribution of isotropic chemical shifts, reflecting a wide distribution of local environments.

2.4.2 Multiple Quantum Magic Angle Spinning – MQMAS

The MQ-MAS experiment is a two dimensional echo experiment which in one dimension is not influenced by second-order quadrupolar broadening. Using the angular dependent terms in the resonance frequency expansion of symmetric (-m ↔ + m) transitions that depend on the quantum coherence order p (defined as the difference between the quantum numbers of two Zeeman eigenstates) the frequency of the –m to m transition is given by [47-,48]

$$\omega_{-m\leftrightarrow+m} = p\omega_0 + \frac{\omega_Q^2}{\omega_0}\left[A_0 C_0^I(p) + A_2(\beta,\varphi) C_2^I(p) P_2(\cos\theta) + A_4(\beta,\varphi) C_4^I(p) P_4(\cos\theta)\right] \quad \textbf{(32)}$$

In this expression, A_0 represents the quadrupolar isotropic shift, while A_2 and A_4 are orientatinally dependent terms responsible for residual line broadening. θ is the angle between the rotor axis and the external magnetic field, and P_2 and $P_4$are the second and fourth order Legendre polynomials.[42]

$$\boldsymbol{P_2(\cos\theta) = \frac{1}{2}(3cos^2\theta - 1)}$$
$$\boldsymbol{P_4(\cos\theta) = \frac{1}{8}\,(35cos^4\theta - 30cos^2\theta + 3)} \quad \textbf{(33)}$$

Under magic-angle spinning conditions, the average of the second order Legendre polynomial is zero and the coefficients $\boldsymbol{C_0^I}$and$\boldsymbol{C_4^I}$are defined by [42]

$$\mathbf{C_0^I(p) = p\left[I(I+1) - \frac{3}{4}p^2\right]}$$
$$\mathbf{C_4^I(p) = p\left[18I(I+1) - \frac{17}{2}p^2 - 5\right]} \quad \textbf{(34)}$$

The residual broadening (arising from the A_4 term) can be removed by a pulse sequence shown in **Figure 5**.[49]

Figure 5 - Pulse sequence scheme and the coherence path using the z-filter.

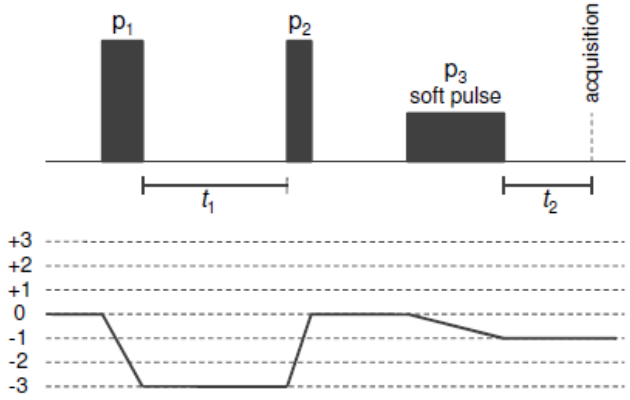

Source: Adapted from AMOUREUX. [50]

Choosing asymmetric coherence path by means of the three-pulse z-filter sequence phase problem and line shape distortion can be largely avoided.[50] The first

pulse is responsible for exciting all possible coherences under the MAS-Hamiltonian.[50] These coherences evolve during the evolution time defined by t_1. The second pulse refocuses these coherences along p = 0 where symmetric coherences (± p) are selected by an appropriate phase cycle. [50] Finally, the third pulse converts this zero-quantum coherence to observable magnetization (single quantum coherence) necessary for signal detection.[50] The two symmetric transitions are correlated and an isotropic echo is detected under the following conditions [34]

$$\mathbf{C_4^I(p)t_1 + C_4^I(-1)t_2 = 0}$$
$$\mathbf{t_2 = \left|\frac{C_4^I(p)}{C_4^I(-1)}\right| t_1 = R(I,p)t_1} \qquad \textbf{(35)}$$

If the acquired signal is subjected to Fourier transformation in both dimensions ($t_1$and t_2). The spectra displayed along the F'$_1$ and F'$_2$dimensions still contain anisotropic contributions. This can be avoided by performing a shearing transformation, effecting a phase correction for all points prior to Fourier transformations along F_1[47]

$$\mathbf{\delta_{F_1} = \delta_{F_1'} + \delta_{F_2'}.R\,(I,p)} \qquad \textbf{(36)}$$

In the sheared spectra, the spectra in the isotropic dimension are still influenced by the second-order quadrupolar shift, which is given by [47]

$$\mathbf{\delta_Q = -\frac{\left(\frac{e^2\,q\,Q}{h}\right)^2 (3+\eta^2)}{10\,\omega_L[2I\,(2I-1)]^2}} \qquad \textbf{(37)}$$

The numerator of eq. (37) can be abbreviated with 3(SOQE)^2, using the definition [34]

$$\mathbf{SOQE = C_q\left(\sqrt{1+\eta^2/3}\right)} \qquad \textbf{(38)}$$

As illustrated in reference for I = 3/2 SOQE and δ_{iso} can be separated by comparing the centers of gravity of the projections in the F_1 and F_2 dimensions.[47]

$$\boldsymbol{\delta_{F1} = \frac{34\delta_{CS}^{ISO} - 60\delta_Q}{9}} \qquad \textbf{(39)}$$

$$\boldsymbol{\delta_{F2} = \delta_{CS}^{ISO} + 3\delta_Q}$$

2.4.3 Rotational Echo Double Resonance – REDOR

Rotational echo double resonance (REDOR) provides a direct measurement of heteronuclear dipole-dipole coupling between pairs of nuclei under MAS conditions.[51–53]This technique is based on a rotor-synchronized spin echo experiment that would normally lead to refocusing of the heteronuclear dipolar couplings.[54] The Hamiltonian that describes the two heteronuclear spin systems ***I*** and ***S*** under the MAS condition is given by [34]

$$\boldsymbol{\widehat{H_D}(t) = \hbar\, \omega_D(\alpha, \beta, t)\widehat{I_Z}\widehat{S_Z}} \qquad \textbf{(40)}$$

Whereω_D is defined by **Equation 41**.

$$\boldsymbol{\omega_D(\alpha, \beta, t) = \pm d\left(sin^2\beta cos2(\alpha - \omega_r t) - \sqrt{2}sin2\beta cos(\alpha - \omega_r t)\right)} \qquad \textbf{(41)}$$

Here, the$\boldsymbol{\alpha}$ and $\boldsymbol{\beta}$ angles describe the orientation of the internuclear vector between spins ***I*** and ***S***with respect to the rotor axis, $\boldsymbol{\omega_r}$ is defined as the rotor frequency and ***d*** is the dipolar coupling constant given by **Equation 26**. The heteronuclear dipolar Hamiltonian of an I-S spin pair oscillates under the MAS condition and is averaged to zero after one rotor cycle (T_R). The REDOR experiment is based on a sign inversion of H_D caused by coherent 180° pulse trains applied to either the I or the S spins, thereby un-doing the coherent averaging by MAS. [54] Under these conditions the average Hamiltonian under MAS calculated according to [34]

$$\langle \hat{\mathbf{H}}_{\mathbf{D}} \rangle = \frac{\mathbf{1}}{\mathbf{T_R}} \int_{\mathbf{0}}^{\mathbf{T_R}} \hat{\mathbf{H}}_{\mathbf{D}}\,(\mathbf{t})\mathbf{dt} \qquad \textbf{(42)}$$

Is no longer zero.

The REDOR experiment consists basically of two parts as shown in **Figure 6**.

Figure 6 -REDOR experiment shown for four rotor periods. (A) The reference signal is obtained by a rotor synchronized spin-echo experiment. (B) The dipolar interaction is re-introduced by π pulses on the non-observed I-channel. The time development of the heteronuclear dipolar Hamiltonian is also determined in both parts.

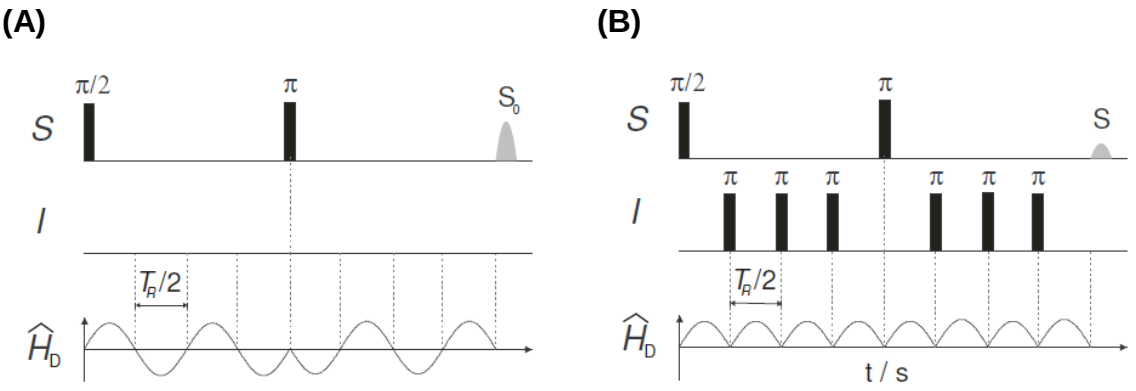

Source: Adapted from DUER.[34]

The first part consists simply of a rotor-synchronized spin-echo experiment, in which the dipolar Hamiltonian is averaged out after one rotor period or several multiples there of (NT_R). The signal intensity S_0 (**Equation 43**) obtained by this reference experiment decays with increasing evolution time due to spin-lattice and spin-spin relaxation. Here, $S_{90°}$is the intensity of the signal after the first pulse. [34]

$$\mathbf{S_0} = \mathbf{S_{90^\circ}} \exp\left[-\frac{\mathbf{NT_R}}{\mathbf{T_2}}\right] \qquad \textbf{(43)}$$

In the second part the heteronuclear dipole-dipole coupling is selectively re-introduced by 180° pulses on the non-observed *I*-channel during multiples of half of rotor periods ($NT_R/2$), with the exception of the point of half the dipolar evolution time. The sign of the dipolar Hamiltonian is inverted by each 180° pulse in the middle of

each rotor period and hence the average dipolar Hamiltonian is no longer cancelled to zero via magic angle spinning. Consequently an additional decay of the signal intensity can be detected which is given by.[34]

$$\mathbf{S} = \mathbf{S_{90^\circ}} \exp\left[-\frac{\mathbf{NT_R}}{\mathbf{T_2}}\right] \cos(\Delta\boldsymbol{\phi}) \qquad \textbf{(44)}$$

where$\boldsymbol{\Delta\phi} = \overline{\boldsymbol{\omega_D \tau_D}}$ is the dephasing angle and $\boldsymbol{\tau_D}$ is the evolution time.The total re-coupling effect results from the integration over the total evolution time, which has to be an even multiple of the rotor period.In a powdered sample the phase in terms of dipolar coupling constant [55-56]

$$\boldsymbol{\Delta\phi} = 4\sqrt{2}\boldsymbol{NT_R d}\,(\boldsymbol{sin\beta cos\beta sin\alpha}) \qquad \textbf{(45)}$$

has to be subjected to a powder average, eventually leading to the expression given by **Equation 46** below [34]

$$\frac{\mathbf{S}}{\mathbf{S_0}} = \frac{\mathbf{1}}{\mathbf{2\pi}} \int_0^{2\pi} \mathbf{d\alpha} \int_0^{\pi} \mathbf{cos(\Delta\phi) sin\beta\, d\beta} \qquad \textbf{(46)}$$

Equation 47 expresses the dephasing effect most conveniently as a normalized difference signal $\boldsymbol{\Delta S/S0}$, the difference between the full ($\mathbf{S_0}$) and the reduced echo (**S**) intensity in the absence and in the presence of recoupling [34]

$$\boldsymbol{\Delta S/S0} = \frac{(\mathbf{S_0} - \mathbf{S})}{\mathbf{S_0}} \qquad \textbf{(47)}$$

From a plot of $\Delta S/S_0$versus the evolution time the strength of the dipolar coupling can be evaluated. For the special case of a system of two spin-1/2 nuclei the dependence of the REDOR difference signal on dipolar evolution time can be described by.[55-56]

$$\frac{\Delta S}{S_0} = 1 - \frac{1}{4\pi}\int_0^{2\pi} d\alpha \int_0^{\pi} \sin\beta \cos(\Delta\phi)\, d\beta \qquad (48)$$

Where $\Delta\phi$ was defined in **Equation 45**.

In case of multiple spin systems the REDOR curves have been shown to be subject to a strong dependence on local geometry.[57-,58] In disordered systems, such as glasses, the spin geometry is generally unknown and may be ill-defined due to a distribution of internuclear distances and bond angles.[59]Using simulation methods with different spin geometries it has been shown that the geometry dependence is slight in the limit of short dipolar evolution timeswhere the REDOR curve can be approximated by a parabola as shown in **Equation 49**.[60]

$$\frac{\Delta S}{S_0} = \frac{16}{15}(NT_R)^2 \sum_{i=1}^{n} d_i^2 \qquad (49)$$

Here the sum of the squares of the dipolar coupling constant is proportional to the heteronuclear dipolar second moment, where ***I*** denotes the spin quantum number of the non-observed nucleus.

$$\frac{\Delta S}{S_0}(NT_R) = \frac{1}{I(I+1)\pi^2} M_2^i (NT_R)^2 \qquad (50)$$

Owing to imperfect π pulses on the non-observe (I-) channel, caused by r.f. inhomogeneities and resonance offset effects experimental REDOR data are frequently subject to systematic errors that reduce the extent of the dephasing relative to the expected dephasing for perfect pulses. Such errors can be compensated by choosing a different reference experiment in which the number of pulses on the I channel is almost the same (see **Figure 7**). Addition of an extra π pulse on the *I*-channel in the middle of the overall dipolar evolution time cancels the re-coupling effect. If imperfections occur their effect will be a diminution of the signal intensity S' that is approximately identical to the diminished reduction the signal intensity S relative to S_0. Thus, a compensated REDOR curve can be obtained by

plotting the sum of $\left(\frac{S_0 - S}{S_0}\right) + \left(\frac{S_0 - S'}{S_0}\right)$, where $\left(\frac{S_0 - S'}{S_0}\right)$ is the experimentally obtained correction due to π pulse imperfections. [61]

Figura 7 -Compensated REDOR pulse sequence.

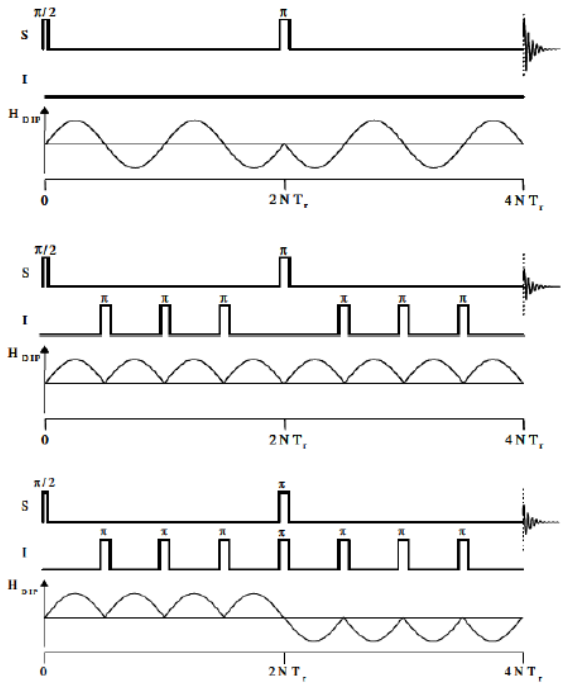

Source: Adapted from DESHPANDE.[42]

2.4.4 Dipolar re-coupling effects nuclear alignment reduction - (DRENAR)

The dipolar re-coupling effects nuclear alignment reduction (DRENAR) is a new useful NMR method developed by J. REN and H. ECKERT providing a selective dipolar coupling strength measurement in multi-spin systems under MAS conditions.[62-63] This technique is based on dipolar recoupling using double quantum excitation. For effecting DQ-excitation the POST-C7 pulse sequence has been shown to be suitable[64]

Figure 8 - DRENAR pulse sequence based on re-coupling by POST-C7 blocks.

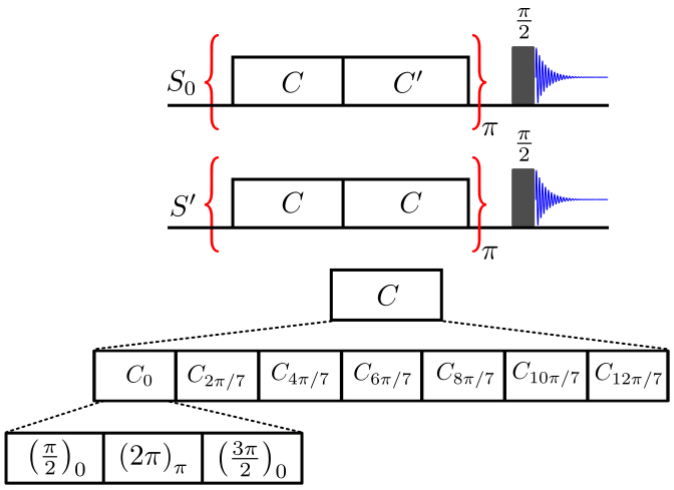

Source: Adapted from REN.[62-63]

In this technique the amplitude of I_z in the DRENAR method rather than the double quantum transfer intensity is being measured. As in REDOR, a difference spectroscopy approach is taken: In the first part of the experiment, the amplitude of the z-magnetization is diminished by two windowless DQ-excitation blocks. In the reference experiment, the overall phases of the pulses in the second block are 90° shifted relative to those of the first block leading to a cancellation of the dipolar recoupling effect. In this way, normalized dipolar dephasing curves can be obtained that are unaffected by relaxation effects. A plot of the normalized difference (S_0-S')/S_0 against the evolution time can be approximated by a parabola as shown in **Equation 51**.[62]

$$\frac{\mathbf{S_0 - S'}}{\mathbf{S_0}} = \frac{\mathbf{0.86\,\pi^2}}{\mathbf{15}}\left(\sqrt{\left(\sum_{\mathbf{k}} \mathbf{b_{jk}^2}\right)\mathbf{NT_r}}\right)^{\mathbf{2}} \qquad \textbf{(51)}$$

Where b_{jk} is the dipolar coupling constant and defined by **Equation 52**. [62]

$$\mathbf{b_{jk}} = \frac{\boldsymbol{\mu_0}}{\mathbf{4\pi}} \frac{\hbar\boldsymbol{\gamma^2}}{\mathbf{2\pi r_{jk}^3}} \quad \textbf{(52)}$$

A parabolic fitting of the DRENAR curves in the initial data range as defined by $\Delta S/S \leq 0.5$ yields values for $\sum_{\mathbf{k}} \mathbf{b_{jk}^2}$. [62]

3 EXPERIMENTAL SECTION

3.1 Synthesis of the Glasses

Commercial reagent grade $Al(PO_3)_3$ (Sigma-Aldrich, 99.98 %), $Ba(PO_3)_2$(Sigma-Aldrich, 99.99 %) AlF_3 (Sigma-Aldrich, 99.99 %) and BaF_2 (Sigma-Aldrich, 99.99 %) were mixed in a mortar to obtain homogeneous mixtures. Intended glass compositions were $[80Ba(PO_3)_2 – 20Al(PO_3)_3]_{1-x}[80BaF_2 – 20AlF_3]_x$ ($0 \leq \mathbf{x} \leq 40$ - mol%).

The mixtures of 10 g were heated at 1100°C and melted for 10 minutes using a resistive furnace open to atmosphere in a platinum crucible with a Pt-cover. The liquid was then poured onto a copper plate ($x \leq 20$mol%) or into liquid nitrogen($x \geq 30$ mol%) to avoid crystallization. Evaporation weight losses wereregularlycheckedand found to amount to ca. 10wt%.

3.2 Thermal Analysis

The glass transition temperatures (T_g) were determined by differential thermal analysis (DTA), using a Netzsch STA 409 C/CD instrument operated at a constant heating rate of 10°C min^{-1}up to 800°C under nitrogen flow (20,0 mL min^{-1}). The temperature difference between the sample and an aluminium oxide crucible used as a reference was recorded.

3.3 X-ray Diffraction

X-ray diffraction experiments were done to confirm the amorphous state using a copper anode (Cu-Kα line, λ = 1.54 Å). Scattering angles (2θ) between 10 and 65° were scanned at a rate of 0.5° min^{-1}.

3.4 Raman Spectroscopy

Raman spectroscopic measurements were conducted on powdered samples with a BrukerSenterra-Raman microscope, which is a dispersive spectrometer. The scattered light from the sample was monochromatized using a mesh with 400 lines per mm and sampled by a CCD detector (1024 x 256 pixels). The excitation was done by a frequency-doubled Nd:YAG laser (532.18 nm) operated at 20 mWpower. Powdered samples were measured with five scans that were co-added using an integration time of 10-20 s in the range between 200 and 1600 cm^{-1}. The spectra were processed using the Opus software.

3.5 Solid-State NMR Spectroscopy

3.5.1 Properties of the Examined Nuclei

Table 1 summarizes the most important properties of the nuclei examined in this work.

Table 1 - Properties of examined nuclei

Nucleus	**^{19}F**	**^{27}Al**	**^{31}P**
Natural Abundance / %	100	100	100
Nuclear Spin Quantum Number	1/2	5/2	1/2
Gyromagnetic Ratio γ / 10^7 rad T^{-1} s^{-1}	25.181	6.976	10.841
ν_L / MHz	188.154 (at 4.70T)	130.287 (at 11.74 T)	202.404 (at 11.74 T)
Reference Substance	$CFCl_3$ AlF_3(s)(-172 ppm)	1 M $Al(NO_3)_3$ aq. (0ppm)	H_3PO_4 85 % (0ppm)

Source: BytheAuthor

3.5.2 Experimental Details of the NMR Measurements

All the solid state NMR measurements were done on Bruker DSX 500, 400 and 200 spectrometers equipped with high-speed magic-angle spinning probes. Data acquisition and processing was done using the TOPSPIN software. Line shape deconvolution and simulationof the spectra obtained were done using the DMFIT program.[65]

3.5.3Single Pulse Experiments

^{19}F solid-state MAS NMR spectra were acquired at 188.15 MHz at a magnetic field strength of 4.65 T, using a 2.5 mm-MAS NMR probe head operated at a typical spinning frequency of 25.0 kHz. The excitation pulses were 3.10 µs in length (corresponding to a 90° flip angle) and a recycle delay of 40 s (> $5.T_1$) was used.

^{31}P and ^{27}Al MAS NMR spectra were acquired at 202.4 and 130.3 MHz, at a field strength of 11.74 T. Samples were spun at 14.0 kHz within a 4 mm MAS NMR probe. Short excitation pulses of 0.30 µs length (corresponding to solid flip angles below 30°) were used for ^{27}Al with a recycle delay of 2 s. For ^{31}P-NMR90° pulses of 3.80 µs and a recycle delay of 80 s (> $5.T_1$) were used.

3.5.4 MQ-MAS NMR Experiments

The three-pulse-z-filtering sequence[50] was used for the ^{27}Al MQ-MAS experiments. These measurements were carried out at 11.74 T, using a 4 mm-MAS probe operated at a rotation frequency of 14.0 kHz. Three-quantum excitation und reconversion pulses of 2-2.5 and 0.7 – 1.0 µs length at a 130 kHz nutation frequency were used. Subsequently single quantum coherence signal was generated by a third, soft pulse (length 9.0 – 11.0 µs) at a nutation frequency of 14.0 kHz. 540 scans were acquired using a recycle delay of 1.0 s. The experimental data were processed using the BRUKER software TOPSPIN and the program XFSHEAR accomplished the “shearing transformation”. From the centers of gravity of the peaks obtained in the F_1 and F_2 dimensions, the isotropic chemical shifts and the “Second Order Quadrupolar Effects” (SOQE) were evaluated using standard analysis procedures.[50]

3.5.5 REDOR Experiments

$^{27}Al\{^{31}P\}$ and $^{19}F\{^{31}P\}$-REDOR experiments were conducted on a BRUKER AVANCE DSX 500 FT-NMR spectrometer (11.74 T) at a spinning frequency of 14.0 kHz and 25.0 kHz, respectively.

The pulse sequence used in this experiments the compensated method proposed by CHAN and ECKERT (see **Chapter 2.4.3**). In the $^{27}Al\{^{31}P\}$-REDOR experiments the 180° pulse lengths for the ^{27}Al observed nuclei were 7.0 – 8.4 µs and recycle delays of 5 s were used. On the ^{31}P channel 180° pulse lengths were 8.40 µs and the pulses were phase cycled according to the XY-4 scheme.[5419]$F\{^{31}P\}$-REDOR experiments were done with 180° pulses of 5.0 µs length for^{19}F and of 3.5 µs length for ^{31}P. For the observe nuclei^{19}F, recycle delays of 5.0 s was used. The pulses on the non-observe ^{31}P channel were phase cycled according the XY-4 scheme.

3.5.6 DRENAR Experiments

The $^{31}P\{^{31}P\}$-DRENAR measurements were carried out on a BRUKER AVANCE DSX 300 spectrometer, at various spinning frequencies from 7.0 to 11.0 kHz, under steady-state conditions (recycle delay 80.s) as described in **Chapter 2.4.4**. One POST-C7 pulse block spans two rotor periods and the ^{31}P nutation frequency is seven times the spinning rate.

4 RESULTS AND DISCUSSION

4.1 XRD Results

The XRD data of the aluminium fluorophosphate glasses in this work are summarized in **Figure 9**. They reveal that completely amorphous samples were obtained for all glass compositions with x ≤ 30. Glass with composition x = 40 shows small reflectionpeaks at 22, 25, 31°, which could be assigned to crystalline β-$Ba(PO_3)_2$.(ICDD-JCPDS index no. 43-0518).Crystallization of this phase was previously observed in barium phosphate glasses with composition $40BaO\text{-}60P_2O_5$.[66] The absence of sharp diffraction peaks arises from the lack of any long range order, which is characteristic of the glassy state. Nevertheless, the maxima at 26° and 41° reflect the existence of short range order.[66]

Figure 9- Powder XRD data of the glass line $[80Ba(PO_3)_2 – 20Al(PO_3)_3]_{1-x}[80BaF_2 – 20AlF_3]_x$ (0 ≤ x ≤ 40 - mol%)examined in the present study.

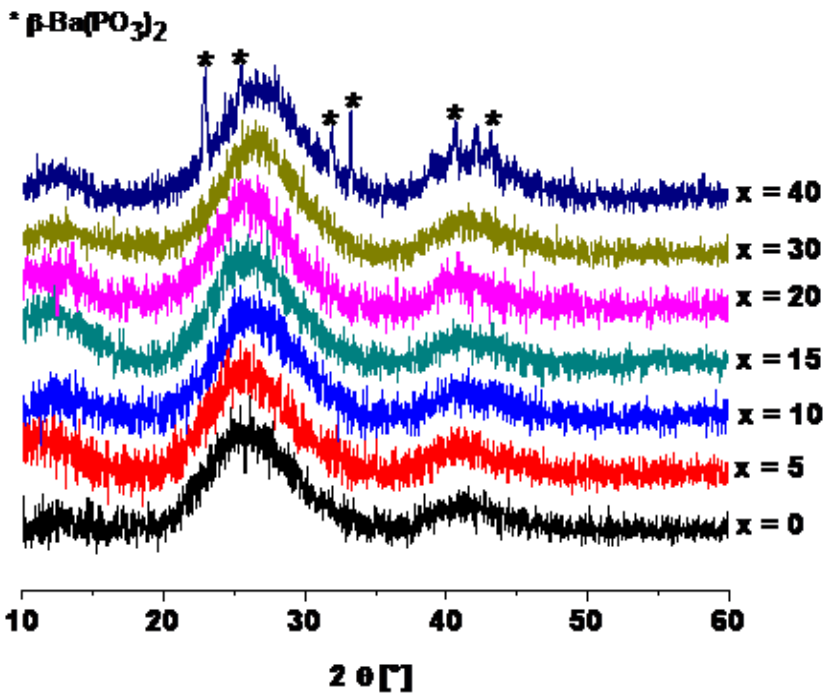

Source: By the Author

4.2 Thermal Analysis

Figure 10 shows are representative DSC curve of a glass sample with composition x = 25, the complete set of measurements is shown in **Appendix 1**. In this figure we can see different thermal events, such as the glass transition (onset temperature 525°C), and the crystallization exotherm (onset point at 636°C). The endothermic transition with the onset temperature at 753°C indicates the onset of melting of the crystallized phase.

Figure 10- Representative DTA curve for the sample composition $[80Ba(PO_3)_2 – 20Al(PO_3)_3]_{75}[80BaF_2 – 20AlF_3]_{25}$. Exothermic events are represented by positive excursions.

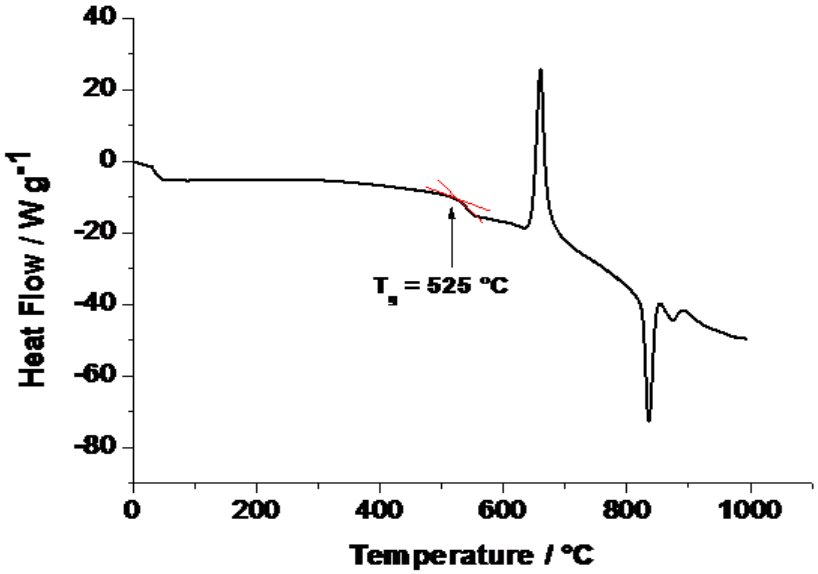

Source:By the Author

The thermal properties, T_g, T_x (onset of crystallization) and $(T_x-T_g)/T_g$ (thermal stability factor) of the different glasses are summarized in **Table 2**.

Table 2– Glass compositions and thermal properties of the glass samples. * partially crystalline

x F / mol%	T_g± 2/ °C	T_x ± 2 / °C	T_x-T_g ± 2 / °C	T_x-T_g/T_g± 0.01
0	492	675	183	0.37
5	489	683	194	0.40
10	506	665	159	0.31
15	520	671	151	0.29
20	511	655	144	0.28
25	525	647	122	0.23
30	545	636	91	0.17
35*	535*	641*	106*	0.20*
40*	540*	599*	59*	0.11*

Source: By the Author

Multiple crystallization peaks were not observed and this suggests that one crystalline phase is being formed.

Intuitively, T_g is expected to decrease with increasing fluorine content, as incorporation of fluoride tends to depolymerize the network.[11,21,67,68]

In the present samples, we observe the opposite effect. As discussed later this observation may be related to the fluoride losses encountered in these samples, which are most likely also accompanied by F/O-exchange in the atmosphere.

The replacement of fluoride by oxide is expected to result in a depolymerization of the phosphate network. Unlike the situation in silicate glasses, the depolymerization in phosphate glasses is actually accomparied by an increase in T_g,which is what observed in the present system.

4.3 Raman Scattering Results

Figure 11 shows the Raman spectra. For glass with x = 0, the bands observed at 1161cm^{-1} and 1251 cm^{-1}are assigned to symmetric and asymmetric PO_2^- stretching modes from Q^2 units, respectively, whereas the band at 688 cm^{-1} is assigned to the symmetric stretching P-O-P modes.[19,21,29] The feature at 340 cm^{-1} has been assigned to pendent PO_2 bending.[20,69]

Figure 11 - Raman spectra of $[80Ba(PO_3)_2 – 20Al(PO_3)_3]_{1-x}[80BaF_2 – 20AlF_3]_x$ ($0 \leq x \leq 30$ - mol%) glasses.

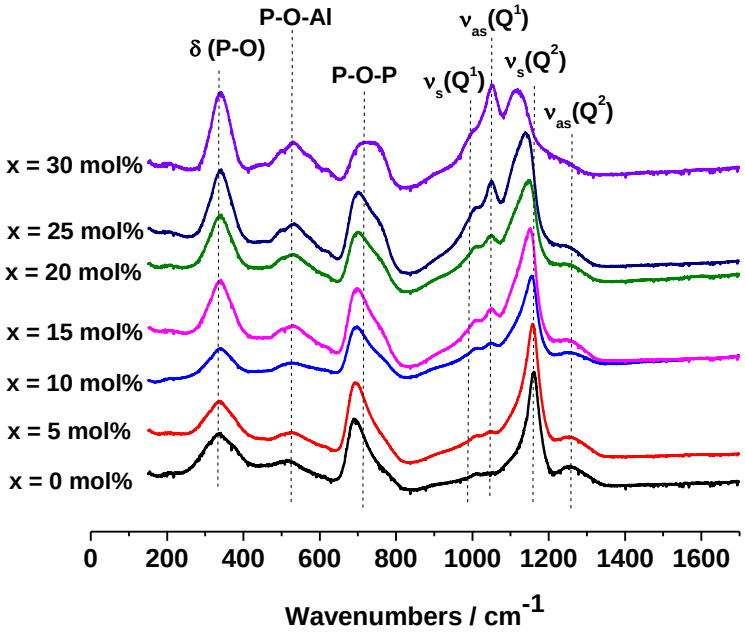

Source:By the Author

With increasing fluoride content, the spectra show a systematic evolution. The feature around 1160 cm^{-1}, characteristic of the $\nu_s(PO_2)$ stretching mode, gradually shifts to lower frequencies. A new peak, observed at 1116 cm^{-1}can be attributed to the asymmetric $Q^1(PO_3^{2-})$ stretching mode. These data indicate that with increasing ***x*** the amount of non-bridging oxygen increases, as the Q^2 units present in the starting materials $Al(PO_3)_3$ and $Ba(PO_3)_2$ are successively converted to Q^1units. As discussed in **Chapter 4.4** this interpretation of the Raman spectra is consistent with the evidence from solid state NMR.

4.4 NMR Results

4.3.1 Fluoride Quantification by ^{19}F NMR

As fluoride losses and/or replacement by oxide species are a common issue in the preparation of oxyfluoride glasses, the total F content was quantified via NMR using a previously described standard addition method.[30] A weighed amount of a well-known standard material is added to a weighed amount of the material being

analyzed and the respective signal areas are compared. NaF was used as the standard material for the x = 20 sample and BaF_2 was used as the standard addition material for the x = 30 sample.

^{19}F MAS-NMR spectra were recorded as rotor synchronized Hahn spin echoes on samples spinning at 25 kHz. A relaxation delay of 250 s was used, which ensured that the spectra were measured under equilibrium (fully relaxed) conditions, yielding rigorously quantitative results.

Figure 12 shows the experimentally observed basis for this quantification. The resonances of the standard and the analyte including their corresponding spinning sidebands were fitted to Gaussian lineshapes and the corresponding areas were quantified. The signal from NaF was fitted (artificially) to two distinct components to account for deviations from perfect Gaussian lineshapes. **Table 3** summarizes all the relevant details, including the results of the ^{19}F peak area deconvolution.

Table3 – Experimental results ofthe 19F NMR quantification and peak deconvolution results

	Weight ± 0.021 / mg	**δ ± 0.5 / ppm**	**fwhm ± 0.5 / ppm**	**Area ± 1 / %**
Standard				
BaF_2	1.553	-13.0 / 12.9	2.8 / 5.9	44 / 22
NaF	0.520	-222.9 / 222.8	4.7 / 11.0	37 / 28
Sample / mol%				
20	14.552	-62.2 / -106.3	13.9 / 59.0	4 / 31
30	15.121	-62.4 / -111.4	11.9 / 50.6	2 / 32

Source:By the Author

Based on the results obtained, only ca. 25% of all the fluorine is retained in both glasses under the preparation conditions used. This analysis is still subject to a

correction accounting for potential T_2 differences between samples and standards, as the two materials may decay with different rates during the evolution period of the rotor-synchronized Hahn spin echo sequence (two rotor periods, ca. 80 µs). Experiments done with an evolution time of 160 µs (4 rotor periods) suggest similar results. Based on this preliminary data, we suggest that the correction for different T_2 values may be neglected in our quantification experiment. As only ca. 10% weight losses were observed after melting, we assume that part of fluoride loss occurs by uptake of oxide from the furnace atmosphere.

Figure 12 - Deconvolution of the single pulse ^{19}F NMR spectra in the fluorine quantification experiment for the samples x = 20 mol% using NaF (sharp peak at -221 ppm) (left) and 30 mol% using BaF_2 (sharp peak at -14.2 ppm) (right) as internal signal intensity reference compounds.

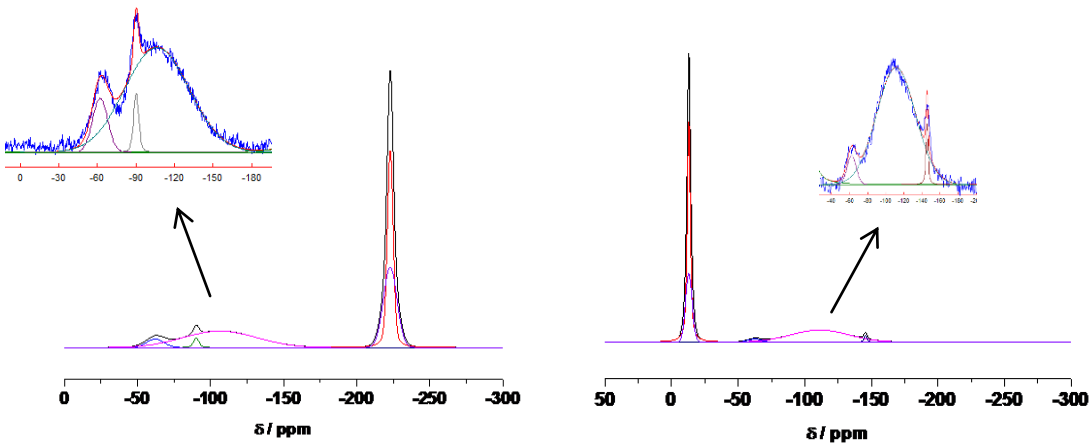

Source: By the Author

4.3.2 Structural Characterization by ^{19}F MAS-NMR

The ^{19}F MAS NMR spectra of the glasses are presented in **Figure 13**.

Figure 13 - ^{19}F MAS-NMR spectra of the glasses measured at 25 kHz.

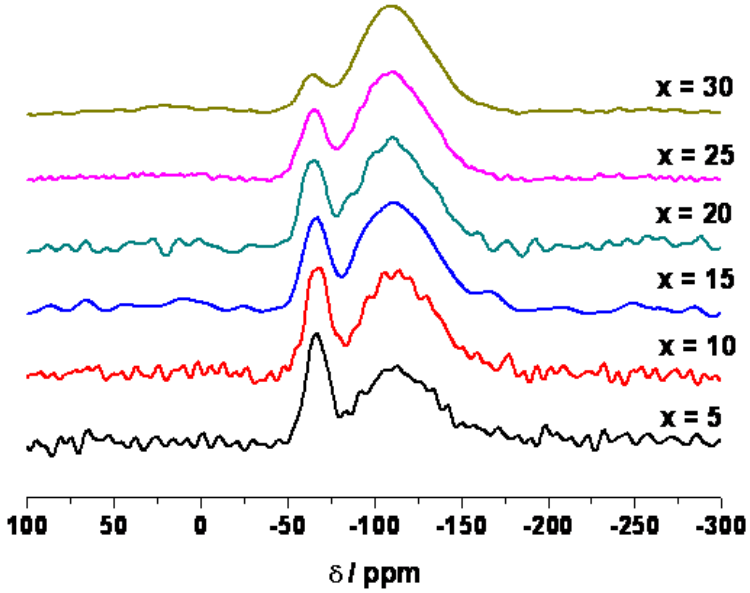

Source:By the Author

Two principal resonances lines are observed near -112.5± 1.5 and -64.5 ± 2.0 ppm. The dominant signal near -112.5 ppm is assigned to fluorine atoms in a mixed alkaline earth/aluminum environment as found in various Al-containing fluorophosphate or fluoride glasses,[28,29,70]and crystalline model compounds.[25,71]The resonance line near -64 ppm is assigned to fluorine atoms bound to phosphorus atoms, based on the observation that the chemical shift of thefluoride site in Na_2PO_3F is -75 ppm.[29,72] This assignment is confirmed by the $^{19}F\{^{31}P\}$-REDOR data described below.

The ^{19}F MAS-NMR spectra are fitted using the DMFIT computer simulation software.[65] These results are listed in **Table 4**. A representative example of the peak deconvolution, done for the sample x = 30 is shown in **Figure 14;** all the other peak deconvolutions are included in **Appendix 2**.

Table 4 – Fitting parameters of the 19F MAS NMR spectra at 4.70 T. δ is the chemical shift, *fwhm* is the full with at half maximum and A_{rel} is relative area

	Al/Ba-F			P-F		
x / mol%	**δ ± 0.5 / ppm**	**fwhm ± 0.5 / ppm**	**A_{rel} ± 1 / %**	**δ ± 0.5 / ppm**	**fwhm ± 0.5 / ppm**	**A_{rel} ± 1 / %**
5	-113.8	54.2	72	-66.6	14.1	28
10	-114.5	53.7	78	-66.4	14.8	22
15	-113.2	59.8	84	-64.9	15.1	16
20	-111.5	49.1	80	-65.5	16.2	20
25	-111.2	50.7	85	-63.5	16.1	15
30	-111.5	50.4	91	-62.4	15.9	9

Source: By the Author

Figure 14 - ^{19}F MAS NMR spectra with simulations where (-) denote P-bonded F species and (-) denote F species in a mixed Ca/Al environment.

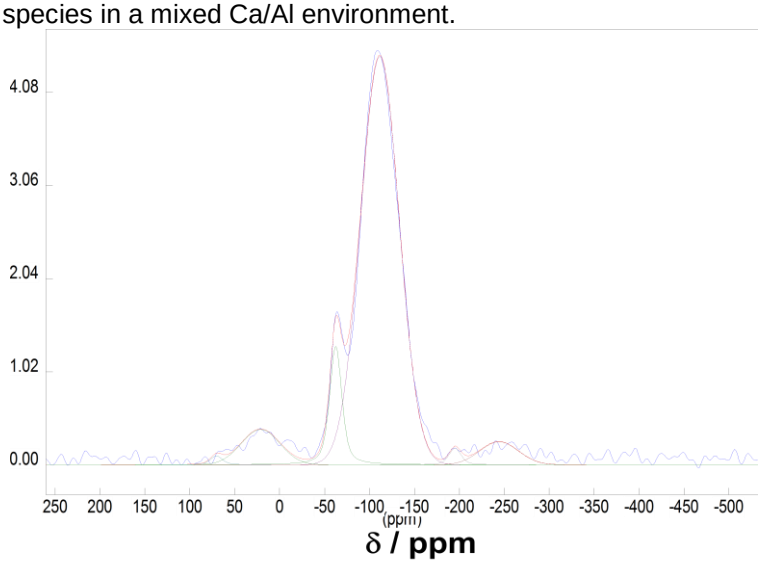

Source:By the Author

Table 5 indicates that the fraction of P-bonded of F atoms decreases systematically with increasing ***x***. This behaviour is generally observed in different preparation methods, e.g sol-gel, of fluorophosphate and aluminophosphate glasses[72,73].

4.3.3 $^{19}F\{^{31}P\}$-REDOR

The $^{19}F\{^{31}P\}$-REDOR experiment was carried out to confirm the assignment of the peak near -62 to -66 ppm to P-bonded fluoride species. The results are shown in **Figure 15**. Unfortunately, a separate REDOR analysis for the two individual components of the line shape deconvolution is not possible here, because the MAS center band of the P-F species overlaps significantly with a spinning sideband of the dominant peak belonging to the Al/Ca-bonded F species. For this reason only the total signal area has been analysed. Part A of **Figure 15** shows the corresponding normalized difference signal ($\Delta S/S_0$) versus dipolar evolution time, suggesting two super imposed individual contributions: a very rapid decay, dominating the initial part of the REDOR curve, and a significantly lower decay dominating the latter part. Part B of this figure shows Fourier Transforms of the S_0 and S signals for the short evolution time of 197 µs. From this **Figure 15** it is clear that the rapidly decaying component can be associated with the signal at -64.5 ppm, whereas the slower decaying component is associated with the signal at -112.5 ppm. For the initial data range ($0 \leq \Delta S/S_0 \leq 0.2$), where the parabolic approximation expressed by **Equation 50** is valid only one data point is available, which is clearly dominated by the P-bonded F species.

Figure 15 - (A): $^{19}F\{^{31}P\}$-REDOR dephasing curve of glass containing 30 mol% (B):^{19}F line shapes for their glass in the absence (red curve) and the presence (black dashed curve) of dipolar dephasing for a fixed dipolar evolution time of 197 µs.

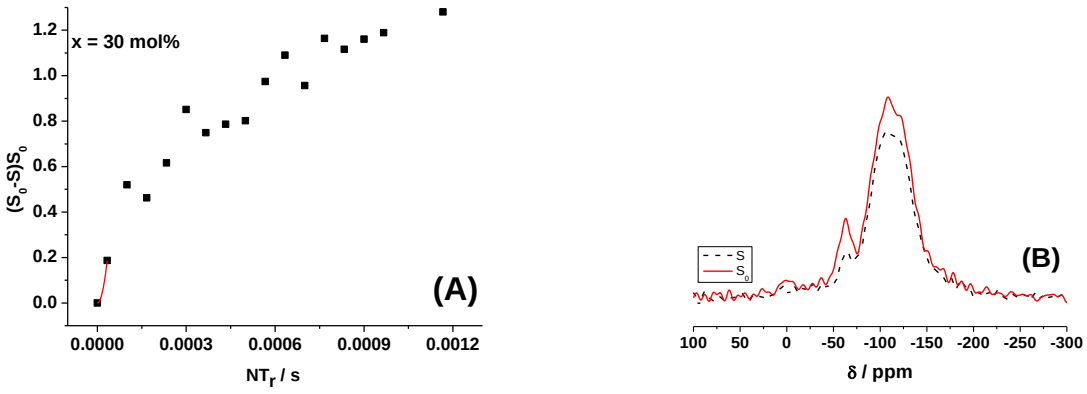

Source:By the Author

The approximate second moment of 1.25 x 10^9rad^2 s^{-2}confirms a very strong heteronuclear dipolar coupling between ^{19}F and ^{31}P, consistent with P-F bonding. From the crystal structure of Na_2PO_3Fa value of 1.01 x 10^9 rad^2 s^{-2} is expected, which is comparable to what is measured here. Even though this one data point analysis is naturally subject to a large error, the steep increase of the REDOR curve in the initial data range is consistent with the occurrence of P-F bonding.

4.3.4 Structural Characterization by ^{27}Al MAS- and MQMAS-NMR

The ^{27}Al MAS NMR spectra are shown in **Figure 16**. Asymmetric and partially resolved lineshapes are observed, which are influenced by both isotropic chemical shifts and second-order quadrupolar perturbations.

Figure 16 - ^{27}Al MAS NMR data measured at 14 kHz and 11.7 T.

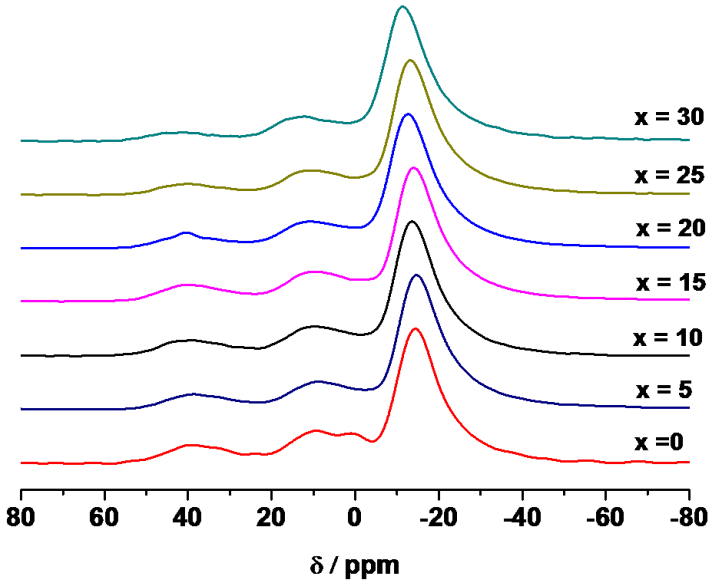

Source: By the Author

The isotropic chemical shift and second-order quadrupolar shifts were separated via ^{27}Al MQ-MAS experiments, using the data analysis procedure described in **Chapter 2.4.2**. In all the samples prepared three distinct resonances are observed with average chemical shifts near 48, 18 and -10 ppm, which are assigned to four-, five- and six-coordinated aluminium species, respectively. **Figure 17** shows

a representative ^{27}Al MQMAS spectrum of the sample with x = 30 and **Table 5** summarizes the results obtained for all the samples.

Figure 17 - ^{27}Al MQ-MAS NMR spectrum of glass with the composition x = 30 measured at 11.7 T.

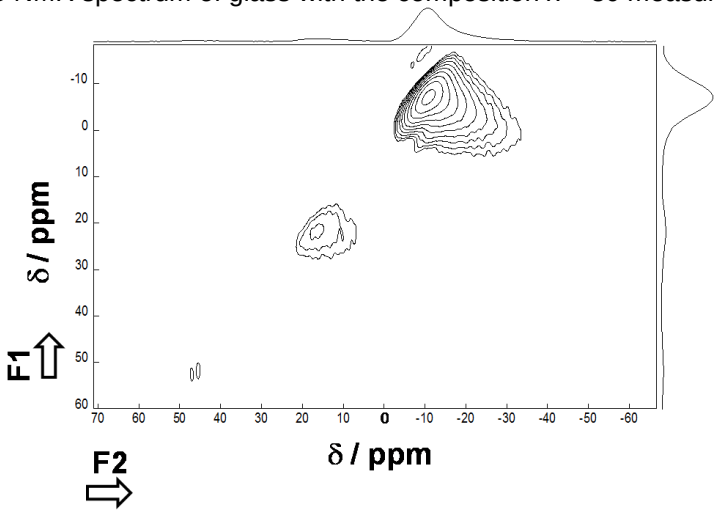

Source:By the Author.

With increasing ***x***, a gradual change of the isotropic chemical shift towards higher frequencies is observed, reflecting the increasing substitution of phosphate by fluoride in the first coordination sphere of the Al species. This effect has been well documented in the literature.[73] In principle further quantification of this effect is possible based on ^{27}Al{^{19}F} and ^{27}Al{^{31}P} REDOR experiments. Below, we report results from the latter measurement.

Table 5 – ^{27}Al chemical shifts and $\mathbf{SOQE} = \mathbf{C_q}\left(\mathbf{1} + {}^{\boldsymbol{\eta^2}}/_{\mathbf{3}}\right)^{1/2}$ obtained from ^{27}Al MQ-MAS

	Al (VI)		Al (V)		Al (IV)	
x / mol%	δ_{cs} ± 1 / ppm	SOQE±0.2/MHz	δ_{cs} ± 1 / ppm	SOQE±0.2 / MHz	δ_{cs} ± 1 / ppm	SOQE±0.2/MHz
0	-11	3.1	16	3.8	47	3.8
5	-10	2.8	16	3.8	47	3.8
10	-10	2.8	16	3.8	47	3.8
15	-10	3.1	16	3.7	48	3.5
20	-10	2.9	18	3.6	48	3.5
25	-10	3.2	18	3.9	49	3.5
30	-9	3.0	19	3.9	50	3.6

Source:By the Author

4.3.5 ^{27}Al{^{31}P}-REDOR

As described above, M_2 (^{27}Al{^{31}P}) values measured via the REDOR technique can be used to quantify the number of Al···P second nearest neighbors in Al-phosphate based glasses.[24,26,74]

In **Figure 18** the results for a fluoride free glass and a glass having the maximum F content are compared. The dipolar second moments (M_2) were obtained from the parabolic fitting in **Equation 47** and the results are summarized in **Table 6**.

Figure 18 - $^{27}Al\{^{31}P\}$ REDOR dephasing curves of glasses with compositions x = 0 (top, right) and x = 30 (bottom, right) and ^{27}Al line shapes for the glasses with compositions x = 0 (top, left) and x = 30 (bottom, left) in the absence (red curve) and the presence (black curve) of dipolar recoupling for a fixed dipolar evolution time of 505 µs and 604 µs, respectively, indicating that the Al environment is affected by dipolar interactions with ^{31}P nuclei.

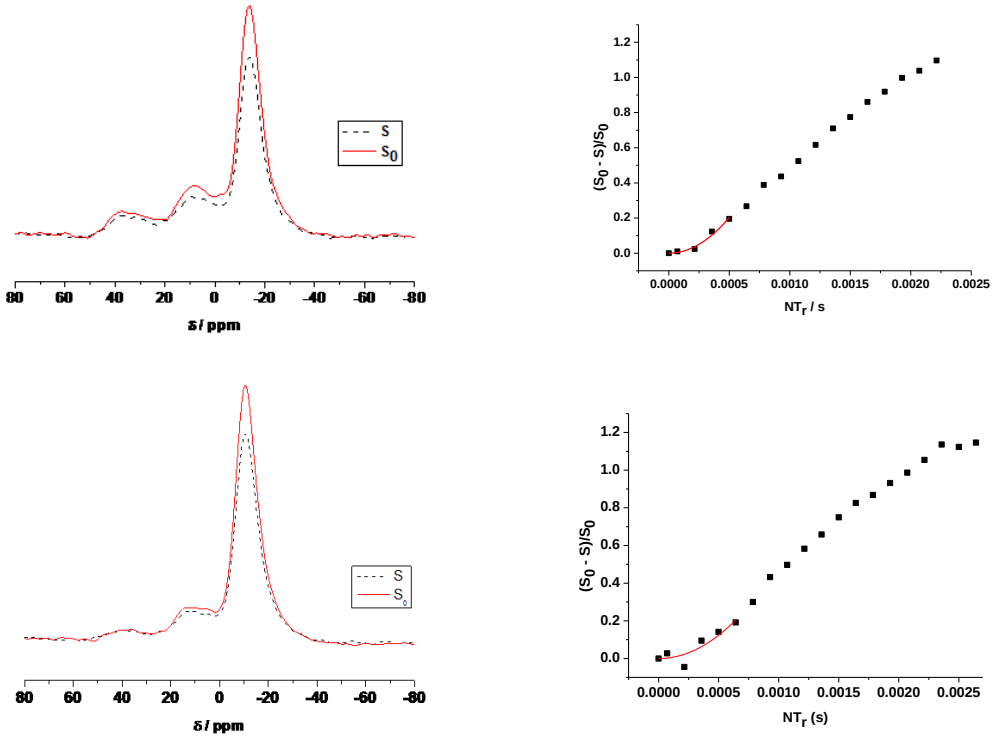

Source: By the Author

Table6 - Second Moment Values $M_2(^{27}Al\{^{31}P\})$ obtained for the Al(VI) units*.*For the $^{27}Al\{^{31}P\}$-REDOR studies, typical errors for the M_2-values are estimated to ± 10%.

Sample	Al(VI)
	$M_2(^{27}Al\{^{31}P\})$ / 10^6 rad^2 s^{-2}
$Al(PO_3)_3$	5.6
0mol%	5.9
10mol%	5.6
20mol%	5.7
30mol%	4.7

Source:By the Author

The $M_2(^{27}Al\{^{31}P\})$ values were obtained only for Al(VI), as the S/N-ratios were too limited for the Al(V) and Al(IV) to get reliable results. **Table 8** illustrates that in all the samples the short-range order of Al is dominated by phosphate species. Only the

sample with the highest F content shows a somewhat weaker REDOR effect, although the data in this sample are more scattered, possibly resulting in lower precision. Thus, the numerical differences in M_2between the different samples are for the most part attributed to random errors.

4.3.6 Structural Characterization by ^{31}P MAS-NMR

Inorder to get information about the phosphate network ^{31}P single pulse experiments were done as shown in **Figure 19**.

Figure 19 - ^{31}P MAS NMR spectra measured at a rotation frequency of 14 kHz. Spinning sidebands are indicated by asterisks.

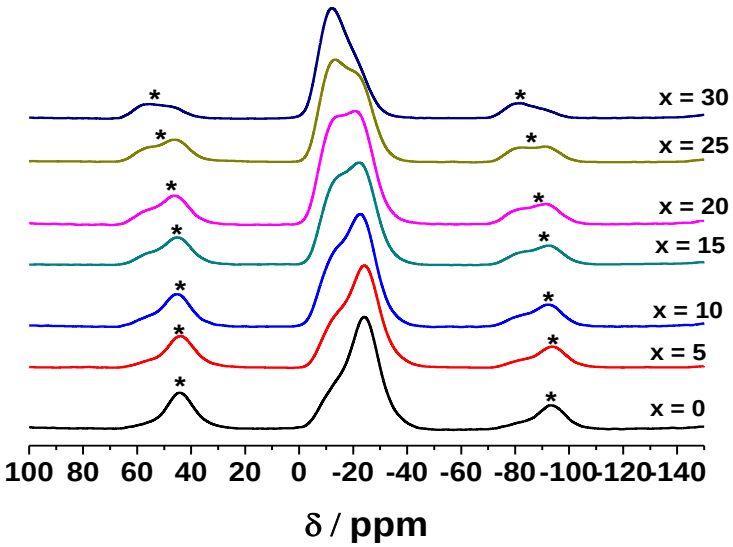

Source:By the Author

These spectra (**Figure 19**) reveal clearly structured signals suggesting the presence of at least two distinct contributions. Typical tentative deconvolutions of the MAS center bands into three Gaussian components are shown in **Figure 20** and **Table 7** summarizes the corresponding parameters.

Figure 20 - ^{31}P MAS NMR spectra with simulations of the x = 0 mol% (left) and x = 30 mol% (right)at 14.0 kHz.

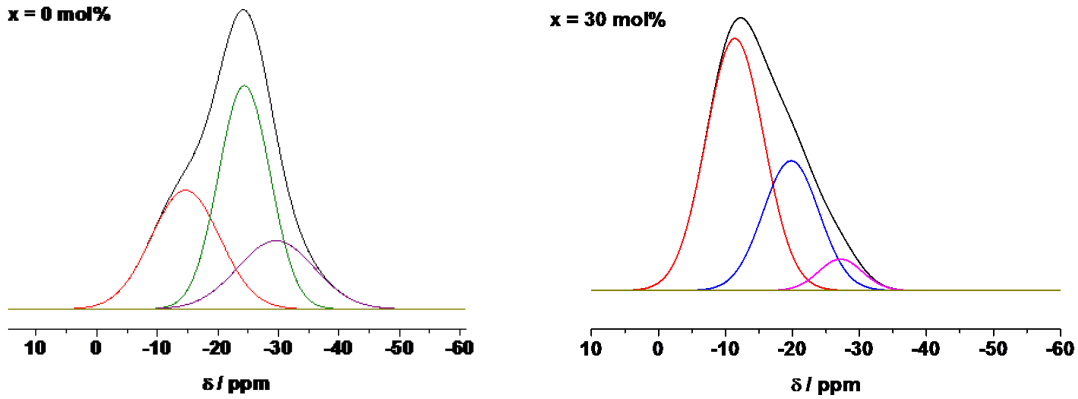

Source: By the Author

Table 7 - ^{31}P MAS-NMR lineshape fitting parameters for [80Ba(PO3)2 – 20Al(PO3)3]1-x[80BaF2 – 20AlF3]x (0 ≤ x ≤ 30) glasses

	Q^1_m			Q^2_0			Q^2_m		
x / mol%	**δ ± 0.5 / ppm**	**fwhm ± 0.5 / ppm**	**A_{rel} ± 1 / %**	**δ ± 0.5 / ppm**	**fwhm ± 0.5 / ppm**	**A_{rel} ± 1 / %**	**δ ± 0.5 / ppm**	**fwhm ± 0.5 / ppm**	**A_{rel} ± 1 / %**
0	-14.7	13.3	28	-24.4	10.0	49	-29.6	14.9	23
5	-13.9	11.8	27	-24.1	10.2	38	-27.5	14.9	35
10	-12.8	11.4	33	-22.8	10.6	46	-27.7	13.4	21
15	-12.8	10.7	37	-22.1	10.3	36	-27.0	12.0	27
20	-11.6	10.3	35	-20.6	10.8	43	-26.9	10.8	22
25	-11.4	9.5	40	-20.2	10.2	41	-26.7	9.4	19
30	-11.4	10.2	63	-19.8	9.8	32	-27.2	7.6	5

Source:By the Author

For the F-free (x = 0) sample the broad asymmetric lineshape can be deconvoluted into three Gaussians located around -14.7, -24.4 and -29.6 ppm (see **Appendix 3**), The phosphate species are identified in terms of the Q^n_mnotation scheme, where *n* denotes the number of connected phosphate (P-O-P linkages) and

m indicates the number of connected aluminium polyhedra. Based on their chemical shifts we can assign these components to Q^2_0(-24.4 ppm), Q^1_m(-14.7 ppm) and Q^2_m(-29.6 ppm) groups. The Q^2_0contribution is consistent with the Raman peak at 1160 cm^{-1} (**Section 6.3**). $Q^1_m$and Q^2_mreflect species with m P-O-Al linkages.Unfortunately, the poor resolution prevents an unambiguous assignment and hence a determination of the number of mixed aluminophosphate species and their quantification proves impossible without any further information. More experimental evidence will be available from future $^{31}P\{^{27}Al\}$-REAPDOR (Rotational Echo Adiabatic Passage Double Resonance) experiments. These couldprovide the number of aluminium atoms connected to each phosphate species.

Concomitant with the increase of ***x***, the fluorine content in the glassy matrix, we can observe a progressive shift of the ^{31}P signal towards higher frequencies and a corresponding increase in intensity of the signal assigned to Q^1_munits. This finding is in agreement with the interpretation of the Raman spectra, suggesting depolymerisation of the polyphosphate network. As described above, we believe that this effect occurs as a consequence of F/O exchange in the furnace atmosphere.

4.3.7 $^{31}P\{^{31}P\}$ – DRENAR

Figure 21shows results from application of the DRENAR method to measure the average strength of the homonuclear^{31}P-^{31}P dipolar coupling.[62,63]

The experimental DRENAR curves measured for the x = 0 and 30samples reveal a significant difference in$\sum_k \mathbf{b_{jk}^2}$.The experimental values of $\sum_k \mathbf{b_{jk}^2}$are determined from a parabolic analysis of the DRENAR curves using the **Equation 52** over the data range $\Delta S/S_0 \leq 0.3$.

Figure 21 - $^{31}P\{^{31}P\}$-DRENAR results for the glasses with compositions x = 0 (top) and x = 30 (bottom). Left parts show the dephasing curves and the corresponding parabolic approximations, while right parts show the corresponding ^{31}PMAS-NMR spectra in the presence and absence of the dipolar recoupling at a dipolar mixing time of 570 µs.

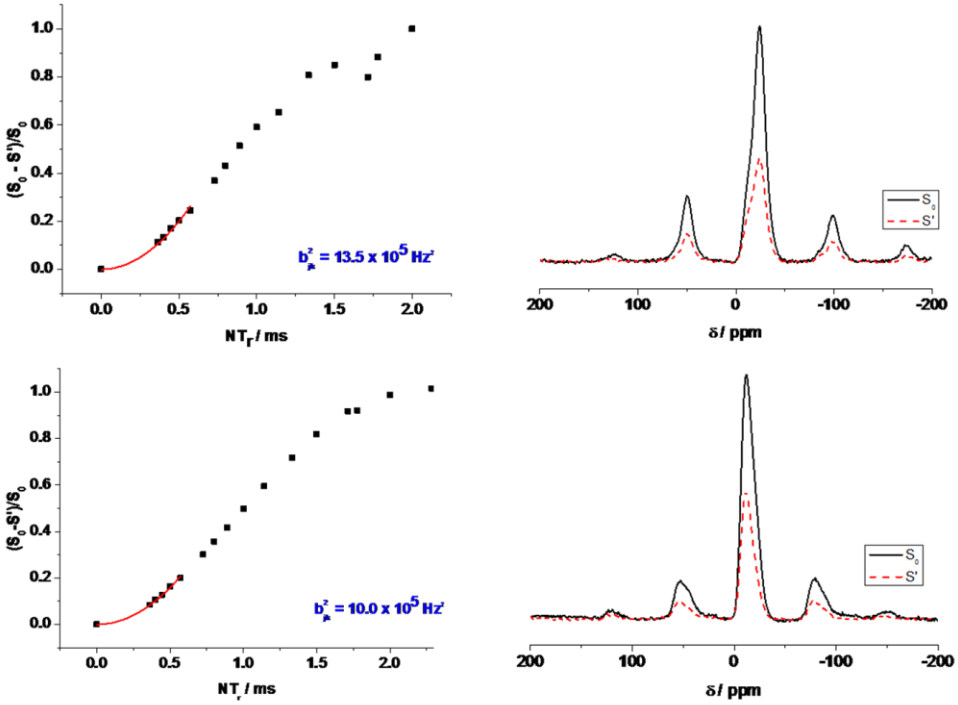

Source:By the Author

The summed squares of the dipolar coupling constants $\Sigma_k b^2_{jk}$ obtained are 13.5 x 10^5 $Hz^2$and 10.0 x 10^5 $Hz^2$for the x = 0 and x = 30 samples, respectively. In phosphate-based systems, squared dipolar coupling constant sums (or M_2 value for that matter) are largely dominated by the average number of P-O-P linkages. Thus, the crystalline reference compound KPO_3(2 P-O-P linkages) has a theoretical $\Sigma_k b^2_{jk}$ of 15.0 x 10^5 Hz^2 characteristic of Q^2 units while the crystalline reference compound $Li_4P_2O_7$(Q^1 units, one P-O-P linkage only) has a theoretical $\Sigma_k b^2_{jk}$ value of 8.5 x 10^5 Hz^2. Based on these literature data, we can use the measured$\sum \mathbf{b^2_{jk}}$values for our glasses to deduce the Q^1/Q^2 ratios via interpolation. In the glass with x = 0 we obtain 77% Q^2 and 23 % Q^1 and in glass x = 30 we obtain 23% Q^2 and 77% Q^1.These results are roughly consistent with the ^{31}P NMR spectral deconvolution of **Figure 19**, suggesting Q^2/Q^1 ratios of 72:28 and 37:63 for x = 0 and 30, respectively. Deviations

can be attributed to the intrinsic systematic error produced by this particular choice of model compounds.

5 CONCLUSIONS AND PERSPECTIVES

The results in this work, along with studies to be planned for the future can be summarized as follows:

i. XRD and DSC data confirm that the batch compositions chosen in this theses result in bulk glasses for x ≤ 30. However, ^{19}F NMR signal quantification studies suggest significant fluoride loss and/or fluoride/oxide ligand exchange. Improved synthesis methods are clearly needed. Subjecting these glasses to a re-fluorination process by re-melting with NH_4-HF_2will be explored in the future. Alternatively, melting of the glasses within metal containers tightly sealed by welding might prove an alternative.[70]

ii. Both Raman and ^{31}P MAS NMR data indicate gradual conversion of Q^2_m units to Q^1_m units with increasing x. Future studies will have to discuss whether this effect is only a consequence of F/O exchange in the melt or if it also happens in the absence of this process.

iii. ^{19}F MAS NMR spectra indicate fluorine atoms in two distinct chemical environments bonded either covalently to P-atoms or situated in a mixed Al/Ba environment. The assignment of the P-bonded F atoms is independently confirmed by$^{19}F\{^{31}P\}$-REDOR .The effect of the P-bonded F species on the functional properties of rare-earth doped laser glasses needs to be studied in the future.

iv. ^{27}Al NMR shows dominantly six-coordinated aluminium, and the $^{27}Al\{^{31}P\}$-REDOR data suggest nearly exclusive coordination of Al with phosphate species. More quantitative information about the phosphate environments will be available from $^{31}P\{^{27}Al\}$-REAPDOR experiments, which are under consideration for future studies.

v. Rare-earth doped glasses need to be investigated to explore the effect of the F/Phosphate ratio on the photophysical properties of the emitting species Furthermore, the crystallization of these glasses to yield glass-ceramics must be explored for the potential design of rare-earth doped ceramic emitters.

REFERENCES

1 EHRT, D.; EBELING, P.; NATURA, U. UV Transmission and radiation-induced defects in phosphate and fluoride–phosphate glasses. **Journal of Non-Crystalline Solids**, v. 263–264, p. 240–250, Mar. 2000.

2 GAN, F. Optical properties of fluoride glasses: a review. **Journal of Non-Crystalline Solids**, v. 184, p. 9–20, May 1995.

3 EHRT, D. Fluoroaluminate glasses for lasers and amplifiers. **Current Opinion in Solid State and Materials Science**, v. 7, n. 2, p. 135–141, Apr. 2003.

4 LUCAS, J.; SMEKTALA, F.; ADAM, J. L. Fluorine in optics. **Journal of Fluorine Chemistry**, v. 114, n. 2, p. 113–118, Apr. 2002.

5 VARSHNEYA, A. K. **Fundamentals of inorganic glasses**. Boston: Academic Press, 1993.

6 RAO, K. J. **Structural chemistry of glasses**. Amsterdam ; New York: Elsevier Science, 2002.

7 ZALLEN, R. **The physics of amorphous solids**. New York: Wiley-VCH, 1983.

8 MCQUARRIE, D. A.; SIMON, J. D. **Molecular thermodynamics**. Sausalito, Calif: University Science Books, 1999.

9 ZHANG, M. et al. Variation of glass transition temperature, Tg, with average coordination number, <m>, in network glasses: evidence of a threshold behavior in the slope |dTg/d<m>| at the rigidity percolation threshold (<m> = 2.4). **Journal of Non-Crystalline Solids**, v. 151, n. 1–2, p. 149–154, Dec. 1992.

10 MICOULAUT, M.; PHILLIPS, J. C. Onset of rigidity in glasses: from random to self-organized networks. **Journal of Non-Crystalline Solids**, v. 353, n. 18–21, p. 1732–1740, June 2007.

11 NAZABAL, V. et al. Fluoride and oxyfluoride glasses for optical applications. **Journal of Fluorine Chemistry**, v. 134, p. 18–23, Feb. 2012.Special issue: Fluorine Chemistry in France.

12 DOUALAN, J. L. et al. Excited-state absorption and up-conversion losses in the Nd-doped glasses for high-power lasers. **Physical Review B**, v. 62, n. 7, p. 4459–4463, Aug. 2000.

13 TICK, P. A. et al. Transparent glass ceramics for 1300 nm amplifier applications. **Journal of Applied Physics**, v. 78, n. 11, p. 6367–6374, Dec. 1995.

14 DEJNEKA, M. J. The luminescence and structure of novel transparent oxyfluoride glass-ceramics. **Journal of Non-Crystalline Solids**, v. 239, n. 1–3, p. 149–155, Oct. 1998.

15 SHIRAKAWA, A. et al. Diode-pumped mode-locked Yb^{3+}:Y^2O^3 ceramic laser. **Optics Express**, v. 11, n. 22, p. 2911, Nov. 2003.

16 TOKURAKAWA, M. et al. Diode-pumped ultrashort-pulse generation based on Yb^{3+}:Sc_2O_3 and Yb^{3+}:Y_2O_3 ceramic multi-gain-media oscillator. **Optics Express**, v. 17, n. 5, p. 3353–3361, Mar. 2009.

17 WEBER, M. J. Science and technology of laser glass. **Journal of Non-Crystalline Solids**, v. 123, n. 1–3, p. 208–222, Aug. 1990.

18 STEVIC, S.; ALEKSIC, R.; BACKOVIC, N. Influence of fluorine on thermal properties of fluorophosphate glasses. **Journal American Ceramics Society**, v. 70, n. 10, p. 264-265, Oct. 1987.

19 KONIDAKIS, I. et al. Structure and properties of mixed strontium−manganese metaphosphate glasses. **Journal of Physical Chemistry C**, v. 114, n. 19, p. 9125–9138, May 2010.

20 NELSON, B. N.; EXARHOS, G. J. Vibrational spectroscopy of cation-site interactions in phosphate glasses.**Journal of Chemical Physics**, v. 71, n. 7, p. 2739–2747, Oct. 1979.

21 MÖNCKE, D.; EHRT, D. Structure and properties of mixed phosphate and fluoride glasses. **Physics and Chemistry of Glasses**, v. 46, n. 2, p. 67–71, Apr. 2005.

22 FERNANDES, R. G. et al. Incorporation of PbF_2 into heavy metal oxide borate glasses. structural studies by solid state NMR. **Journal of Physical Chemistry C**, v. 116, n. 10, p. 6434–6445, Mar. 2012.

23 ECKERT, H. Structural characterization of noncrystalline solids and glasses using solid state NMR. **Progress in Nuclear Magnetic Resonance Spectroscopy**, v. 24, n. 3, p. 159–293, July 1992.

24 TSUCHIDA, J. et al. Cation distribution and local order in mixed sodium metaphosphate glasses. **Journal of Physical Chemistry C**, v. 116, n. 46, p. 24449–24461, Nov. 2012.

25 KICZENSKI, T. J.; STEBBINS, J. F. Fluorine sites in calcium and barium oxyfluorides: F-19 NMR on crystalline model compounds and glasses. **Journal of Non-Crystalline Solids**, v. 306, n. 2, p. 160–168, Aug. 2002.

26 WEGNER, S.; VAN WÜLLEN, L.; TRICOT, G. The structure of aluminophosphate glasses revisited: application of modern solid state NMR strategies to determine structural motifs on intermediate length scales. **Journal of Non-Crystalline Solids**, v. 354, n. 15–16, p. 1703–1714, Mar. 2008.

27 TISCHENDORF, B. et al. A study of short and intermediate range order in zinc phosphate glasses. **Journal of Non-Crystalline Solids**, v. 282, n. 2–3, p. 147–158, Apr. 2001.

28 FLETCHER, J. P.; RISBUD, S. H.; KIRKPATRICK, R. J. MAS-NMR structural analysis of barium aluminofluorophosphate glasses with and without nitridation. **Journal of Materials Research**, v. 5, n. 04, p. 835–840, Dec. 1990.

29 MÖNCKE, D. et al. Comparative spectroscopic investigation of different types of fluoride phosphate glasses. **Physics and Chemistry of Glasses - European Journal of Glass Science and Technology Part B**, v. 48, n. 6, p. 399–402, Dec. 2007.

30 CATTANEO, A. S. et al. Structural role of fluoride in the ion-conducting glass system B_2O_3−PbO−LiF studied by single- and double-resonance NMR. **Journal of Physical Chemistry C**, v. 112, n. 28, p. 10462–10471, July 2008.

31 GERLACH, W.; STERN, O. Das magnetische moment des silberatoms. **Zeitschrift für Physik**, v. 9, n. 1, p. 353–355, Dec. 1922.

32 STERN, O. Ein Weg zur experimentellen prüfung der richtungsquantelung im magnetfeld.**Zeitschrift für Physik**, v. 7, n. 1, p. 249–253, Dec. 1921.

33 LEVITT, M. H. **Spin dynamics:** basics of nuclear magnetic resonance. 2nd. ed. Chichester, England; Hoboken, NJ: Wiley, 2008.

34 DUER, M. J. **Introduction to solid-State NMR spectroscopy**. Oxford, UK; Malden, MA: John Wiley & Sons, 2005.

35 ATKINS, P. W.; FRIEDMAN, R. S. **Molecular quantum mechanics**. 5th ed. Oxford; New York: Oxford University Press, 2010.

36 FARRAR, T. C.; BECKER, E. D. **Pulse and Fourier transform NMR:** introduction to theory and methods. New York: Academic Press, 1971.

37 FUKUSHIMA, E.; ROEDER, S. B. W. **Experimental pulse NMR:** a nuts and bolts approach.Reading, Mass.: Westview Press, 1993.

38 ABRAGAM, A. **Principles of nuclear magnetism**. Oxford Oxfordshire; New York: Oxford University Press, 1983.

39 SLICHTER, C. P. **Principles of magnetic resonance**. 3rd ed. Berlin; New York: Springer, 1996.

40 SHAW, D. **Fourier transform N.M.R. spectroscopy**.2nded. Amsterdam; New York; New York: Elsevier Science Ltd, 1987.

41 MUNOWITZ, M. **Coherence and NMR**. New York: Wiley-Interscience, 1988.

42 DESHPANDE, R. **Structural investigation of alumina containing phosphate and silicate glasses by high resolution solid state NMR spectroscopy**. Westfälischen:WilhelmsUniversitätMünster, 2009.

43 ECKERT, H. NMR in solid state chemistry. **Bunsen-Magazin**, v. 5, p. 159–179, Sept. 2008.

44 VAN VLECK, J. H. The dipolar broadening of magnetic resonance lines in crystals. **Physical Review**, v. 74, n. 9, p. 1168–1183, Nov. 1948.

45 LOWE, I. J. Free induction decays of rotating solids. **Physical Review Letters**, v. 2, n. 7, p. 285–287, Apr. 1959.

46 ANDREW, E. R.; BRADBURY, A.; EADES, R. G. Removal of dipolar broadening of nuclear magnetic resonance spectra of solids by specimen rotation. **Nature**, v. 183, n. 4678, p. 1802–1803, June 1959.

47 MEDEK, A.; FRYDMAN, L. Multiple - quantum magic - angle spinning NMR: a new technique for probing quadrupolar nuclei in solids. **Journal of the Brazilian Chemical Society**, v. 10, n. 4, p. 263–277, Aug. 1999.

48 MEDEK, A.; HARWOOD, J. S.; FRYDMAN, L. Multiple-quantum magic-angle spinningNMR: a new method for the study of quadrupolar nuclei in solids. **Journal of the American Chemical Society**, v. 117, n. 51, p. 12779–12787, Dec. 1995.

49 AMOUREUX, J.-P.; FERNANDEZ, C. Triple, quintuple and higher order multiple quantum MAS NMR of quadrupolar nuclei. **Solid State Nuclear Magnetic Resonance**, v. 10, n. 4, p. 211–223, Feb. 1998.

50 AMOUREUX, J.P.; FERNANDEZ, C.; STEUERNAGEL, S. Z-Filtering in MQMAS NMR. **Journal of Magnetic Resonance Series A**, v. 123, n. 1, p. 116–118, Nov. 1996.

51 MARICQ, M. M.; WAUGH, J. S. NMR in rotating solids.**Journal of Chemical Physics**, v. 70, n. 7, p. 3300–3316, Apr. 1979.

52 HAEBERLEN, U.; WAUGH, J. S. Coherent averaging effects in magnetic resonance.**Physical Review**, v. 175, n. 2, p. 453–467, Nov. 1968.

53 PAN, Y.; GULLION, T.; SCHAEFER, J. Determination of C-N internuclear distances by rotational-echo double-resonance NMR of solids. **Journal of Magnetic Resonance (1969)**, v. 90, n. 2, p. 330–340, Nov. 1990.

54 GULLION, T.; SCHAEFER, J. Rotational-echo double-resonance NMR. **Journal of Magnetic Resonance (1969)**, v. 81, n. 1, p. 196–200, Jan. 1989.

55 MUELLER, K. T. Analytic solutions for the time evolution of dipolar-dephasing NMR signals. **Journal of Magnetic Resonance Series A**, v. 113, n. 1, p. 81–93, Mar. 1995.

56 GULLION, T. Introduction to rotational-echo, double-resonance NMR. **Concepts in Magnetic Resonance**, v. 10, n. 5, p. 277–289, Jan. 1998.

57 NAITO, A. et al. Inter- and intra-molecular contributions of neighboring dipolar pairs to the precise determination of interatomic distances in a simple [13C, 15N]-peptide by 13C, 15N-REDOR NMR spectroscopy. **Chemical Physics Letters**, v. 229, n. 4–5, p. 506–511, Nov. 1994.

58 GOETZ, J. M.; SCHAEFER, J. REDOR dephasing by multiple spins in the presence of molecular motion. **Journal of Magnetic Resonance**, v. 127, n. 2, p. 147–154, Aug. 1997.

59 KLINOWSKI, J. **New techniques in solid-stateNMR**. Berlin, Germany, Springer, 2004.

60 BERTMER, M.; ECKERT, H. Dephasing of spin echoes by multiple heteronuclear dipolar interactions in rotational echo double resonance NMR experiments. **Solid State Nuclear Magnetic Resonance**, v. 15, n. 3, p. 139–152, Dec. 1999.

61 CHAN, J. C. C.; ECKERT, H. Dipolar coupling information in multi spin systems: application of a compensated REDOR NMR approach to inorganic phosphates. **Journal of Magnetic Resonance**, v. 147, n. 2, p. 170–178, Dec. 2000.

62 REN, J.; ECKERT, H. DQ-DRENAR: A new NMR technique to measure site-resolved magnetic dipole-dipole interactions in multispin-1/2 systems: theory and validation on crystalline phosphates.**Journal of Chemical Physics**, v. 138, n. 16, p. 164201, Apr. 2013.

63 REN, J.; ECKERT, H. A Homonuclear rotational echo double-resonance method for measuring site-resolved distance distributions in i=1/2 spin pairs, clusters, and multispin systems. **AngewandteChemie International Edition**, v. 51, n. 51, p. 12888–12891, Dec. 2012.

64 HOHWY, M. et al. Broadband dipolar recoupling in the nuclear magnetic resonance of rotating solids: a compensated C7 pulse sequence. **Journal of Chemical Physics**, v. 108, n. 7, p. 2686–2694, Feb. 1998.

65 MASSIOT, D. et al. Modelling one- and two-dimensional solid-state NMR spectra. **Magnetic Resonance in Chemistry**, v. 40, n. 1, p. 70–76, Jan. 2002.

66 PRISON, J. M.; MARTINELLI, J. R. Formation of colloidal phosphorus particles in barium phosphate glasses. **Physics and Chemistry of Glasses**, v. 45, n. 4, p. 268–271, Aug. 2004.

67 DING, J. Y. et al. The properties and structure of Sn-Ca-P-O-F glasses. **Materials Chemistry and Physics**, v. 82, n. 1, p. 61–67, Sept. 2003.

68 NALIN, M. et al. Scandium fluorophosphate glasses: a structural approach. **ComptesRendusChimie**, v. 5, n. 12, p. 915–920, Dec. 2002.

69 GALEENER, F. L.; MIKKELSEN JR., J. C. The Raman spectra and structure of pure vitreous P_2O_5. **Solid State Communications**, v. 30, n. 8, p. 505–510, May 1979.

70 CHAN, J. C. C.; ECKERT, H. High-resolution ^{27}Al–^{19}F solid-state double resonance NMR studies of AlF_3–BaF_2–CaF_2 glasses. **Journal of Non-Crystalline Solids**, v. 284, n. 1–3, p. 16–21, May 2001.

71 ZHENG, A.; LIU, S.-B.; DENG, F. ^{19}F chemical shift of crystalline metal fluorides: theoretical predictions based on periodic structure models. **Journal of Physical Chemistry C**, v. 113, n. 33, p. 15018–15023, Aug. 2009.

72 ZHANG, L.; DE ARAUJO, C. C.; ECKERT, H. A new sol−gel route to aluminum fluoride phosphate glasses: mechanistic investigations by NMR spectroscopy. **Chemistry of Materials**, v. 17, n. 12, p. 3101–3107, June 2005.

73 ZHANG, L.; DE ARAUJO, C. C.; ECKERT, H. Structural role of fluoride in aluminophosphate sol−gel glasses: high-resolution double-resonance NMR studies. **Journal of Physical Chemistry B**, v. 111, n. 35, p. 10402–10412, Sept. 2007.

74 TSUCHIDA, J. et al. Structure of ternary aluminium metaphosphate glasses. **Journal of Physical Chemistry C**, v. 115, n. 44, p. 21927–21941, Nov. 2011.

APPENDIX

A.1 Thermal Analysis

Figure 1 - DTA curve (red and green) of the fluorophosphate glasses in the $[80Ba(PO_3)_2 – 20Al(PO_3)_3]_{100-x}[80BaF_2 – 20AlF_3]_x$ series.TGA curve (blue). Exothermic events are represented by positive excursions.

x = 0 mol%

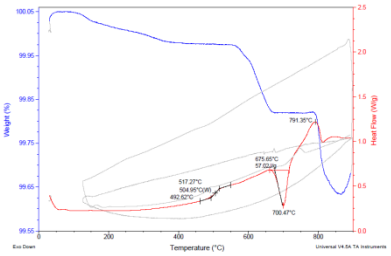

x = 5 mol%

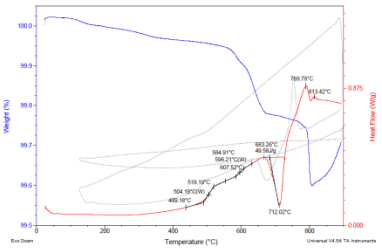

x = 10 mol%

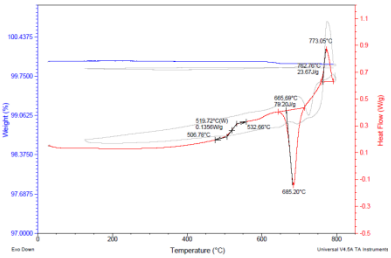

x = 15 mol%

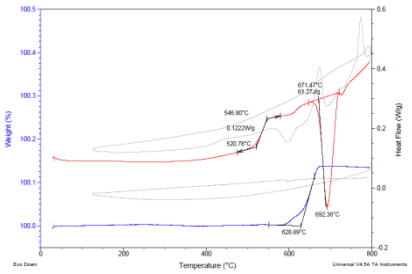

x = 20 mol%

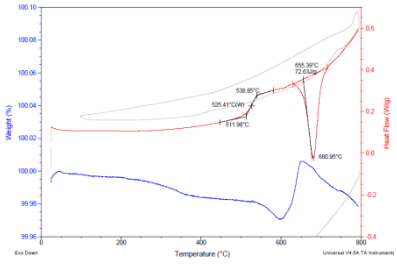

x = 30 mol%

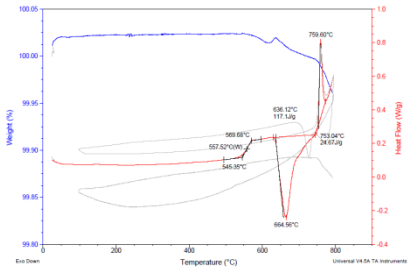

x = 35 mol%

x = 40 mol%

continue

continuation

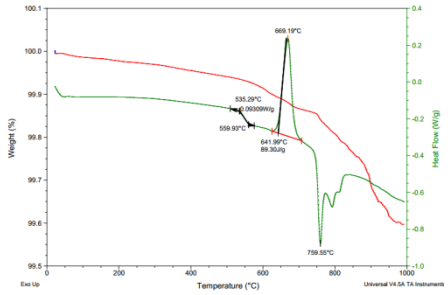

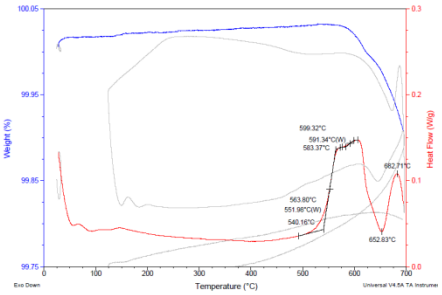

Source:By the Author

A.2. ^{19}F MAS NMR spectrum deconvolutions

Figure 2. - ^{19}F MAS NMR spectrum with simulations of the glasses $[80Ba(PO_3)_2 – 20Al(PO_3)_3]_{100-x}[80BaF_2 – 20AlF_3]_x$ series.

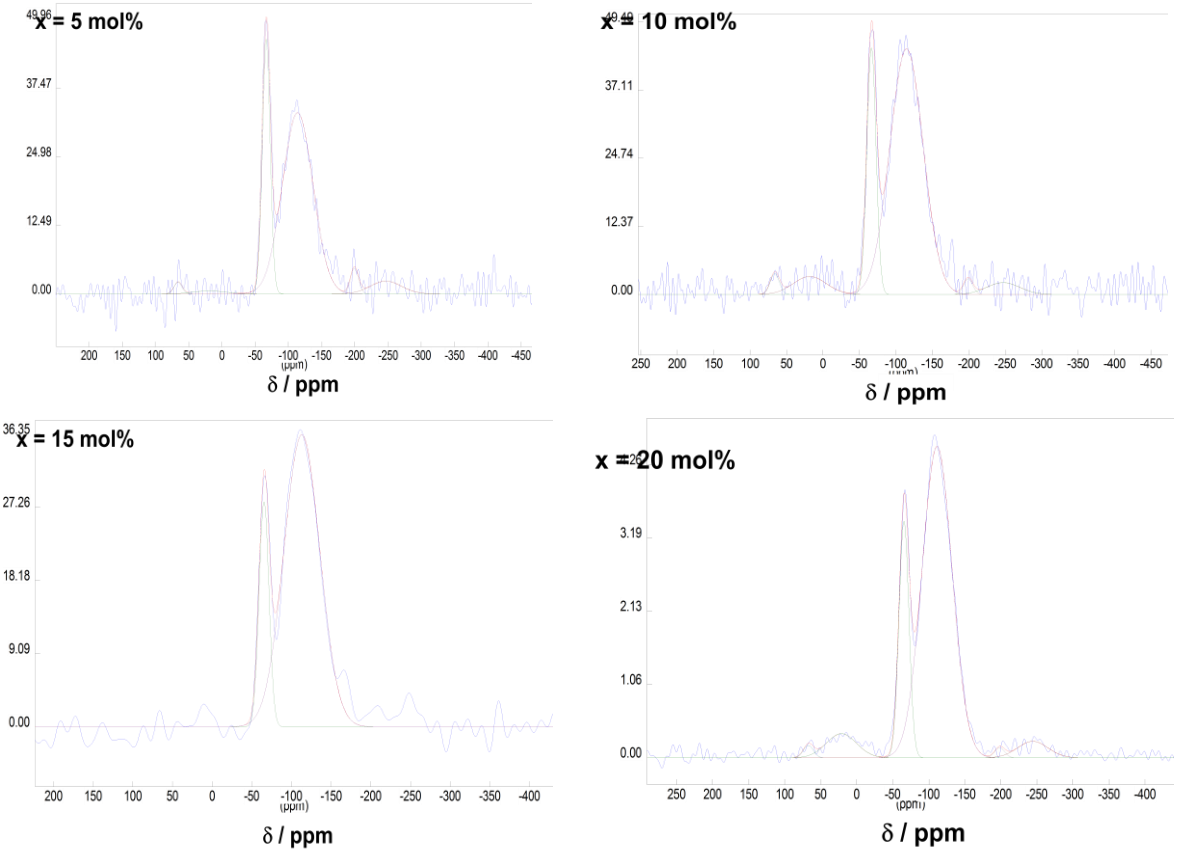

continue

continuation

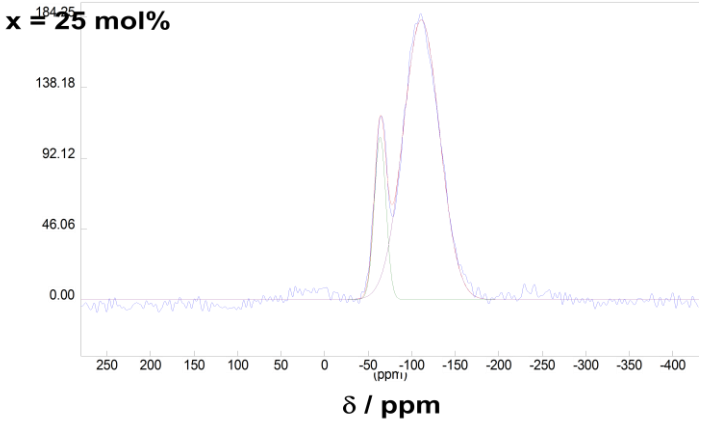

Source: By the Author

A.3. ^{27}Al MQ-MAS NMR

Figure 3 – (A)(B)(C)(D)(E)(F) are the ^{27}Al MQ-MAS NMR spectra of fluorophosphate glasses in the $[80Ba(PO_3)_2 – 20Al(PO_3)_3]_{100-x}[80BaF_2 – 20AlF_3]_x$ series.

(A) x = 0 mol%

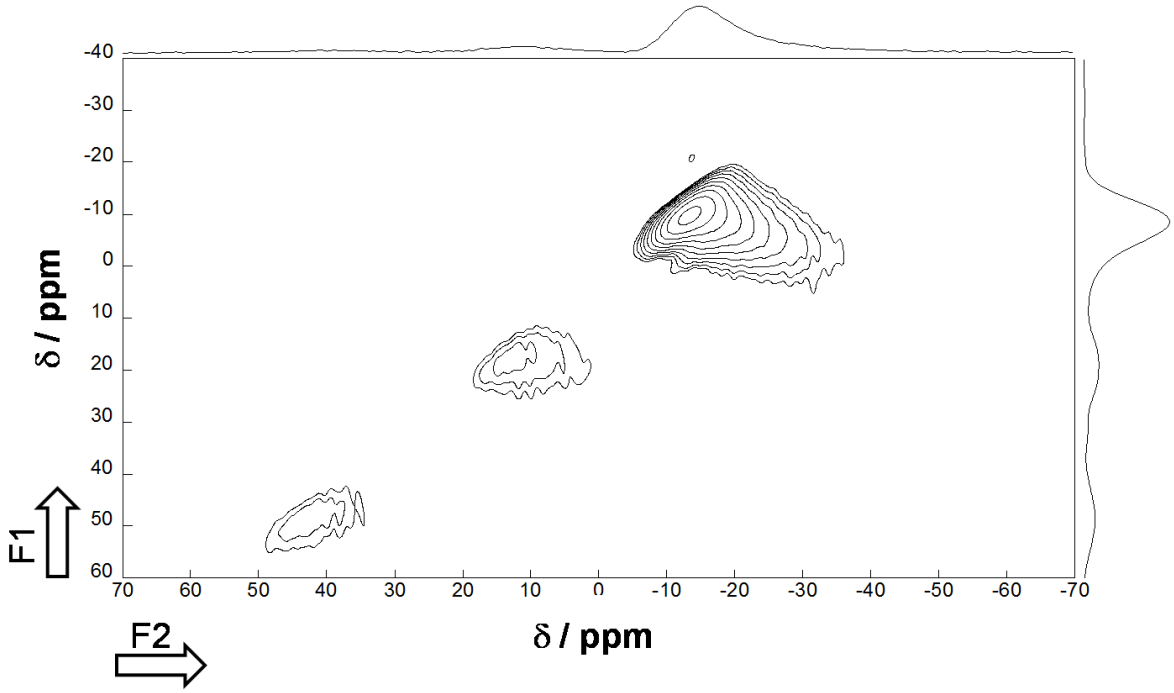

continue

continuation

(B) x = 5 mol%

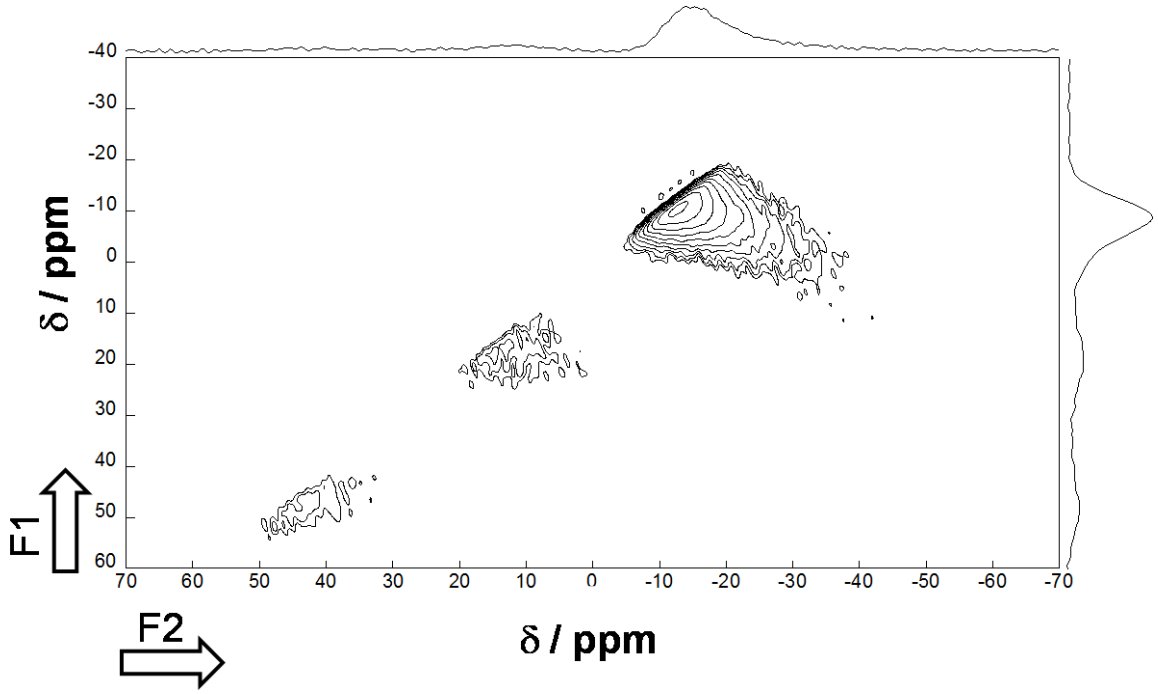

(C) x = 10 mol%

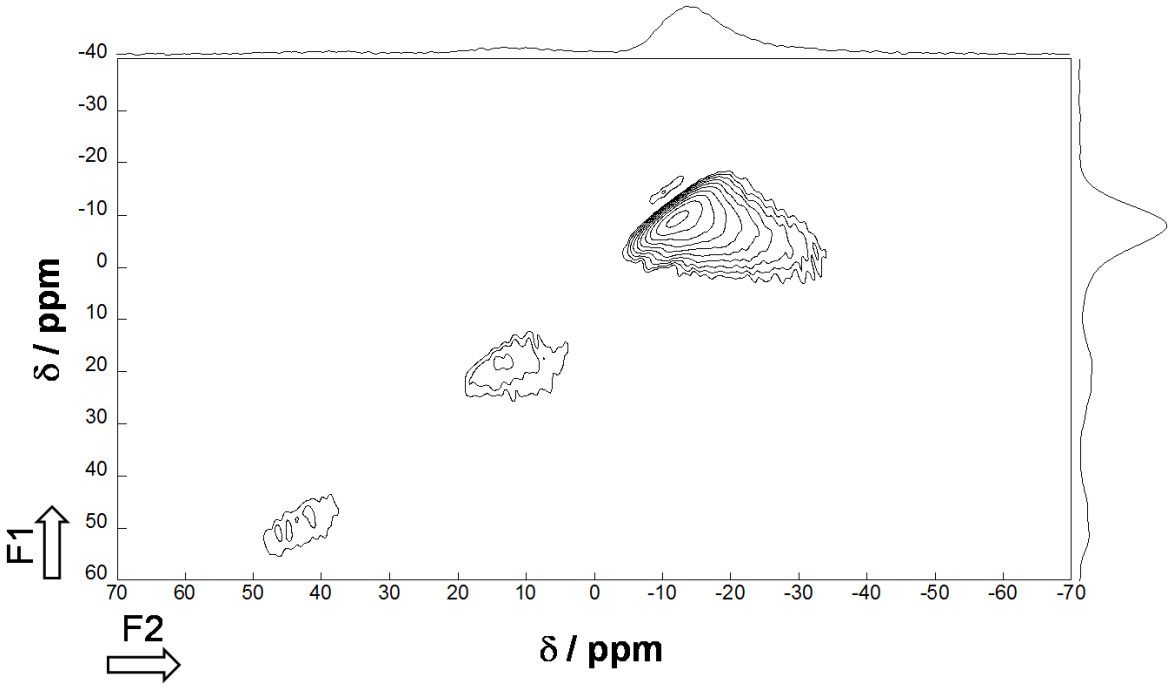

continue

continuation

(D) x = 15 mol%

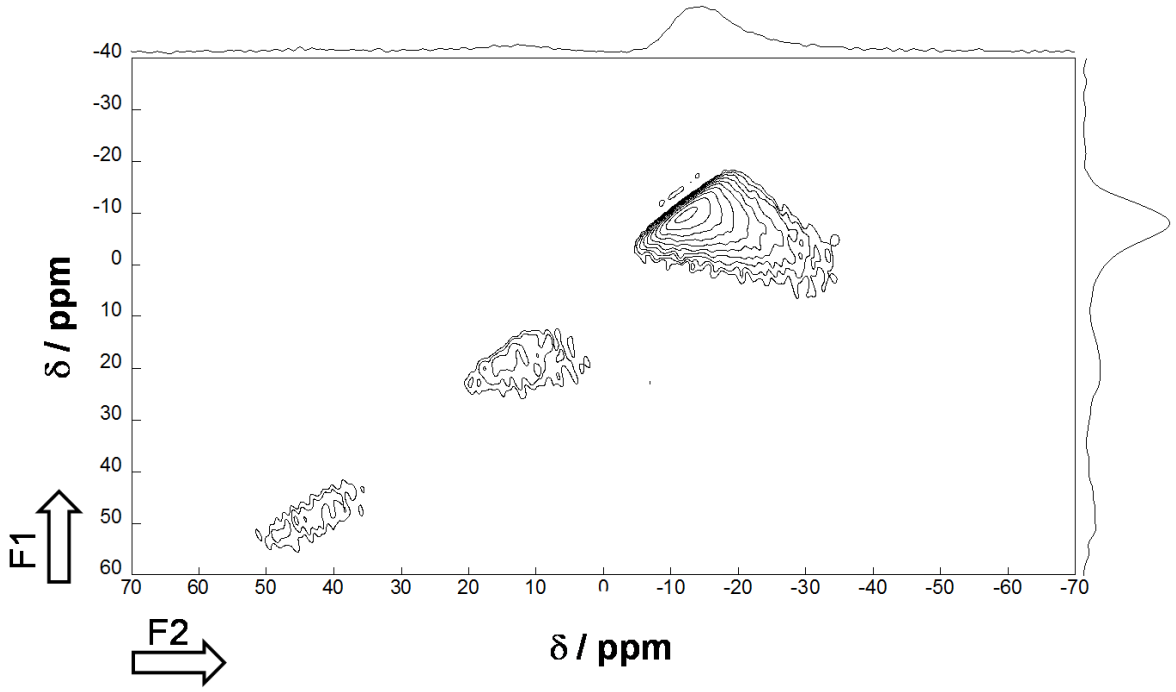

(E) x = 20 mol%

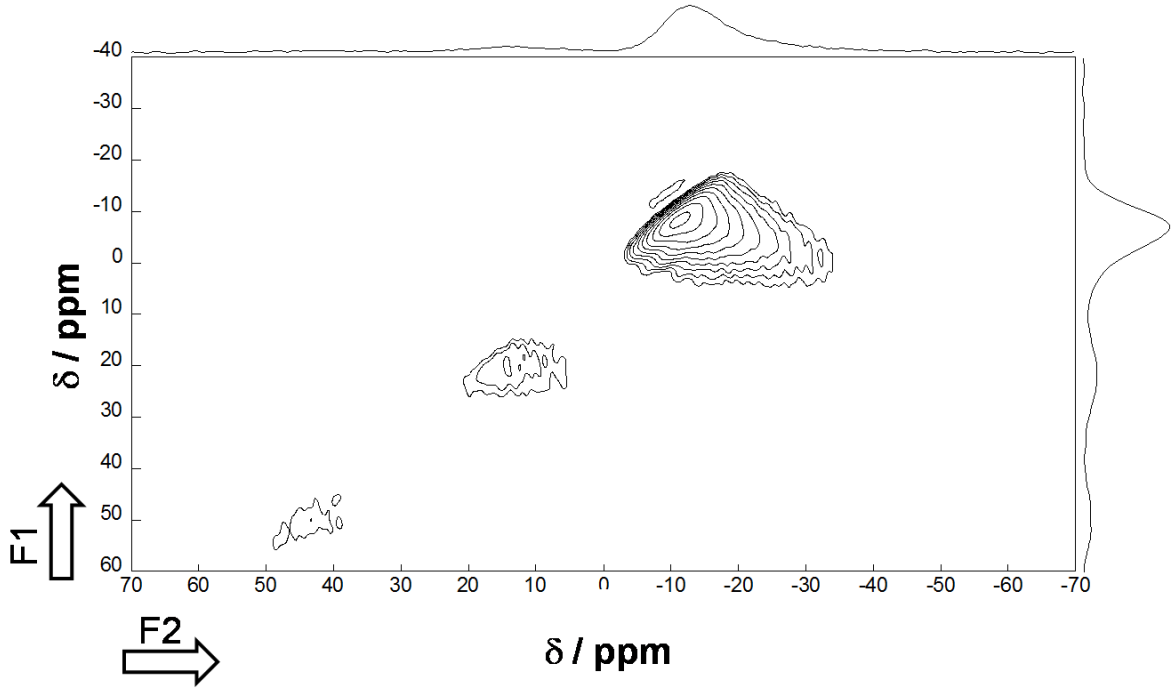

continue

continuation

(F) x = 25 mol%

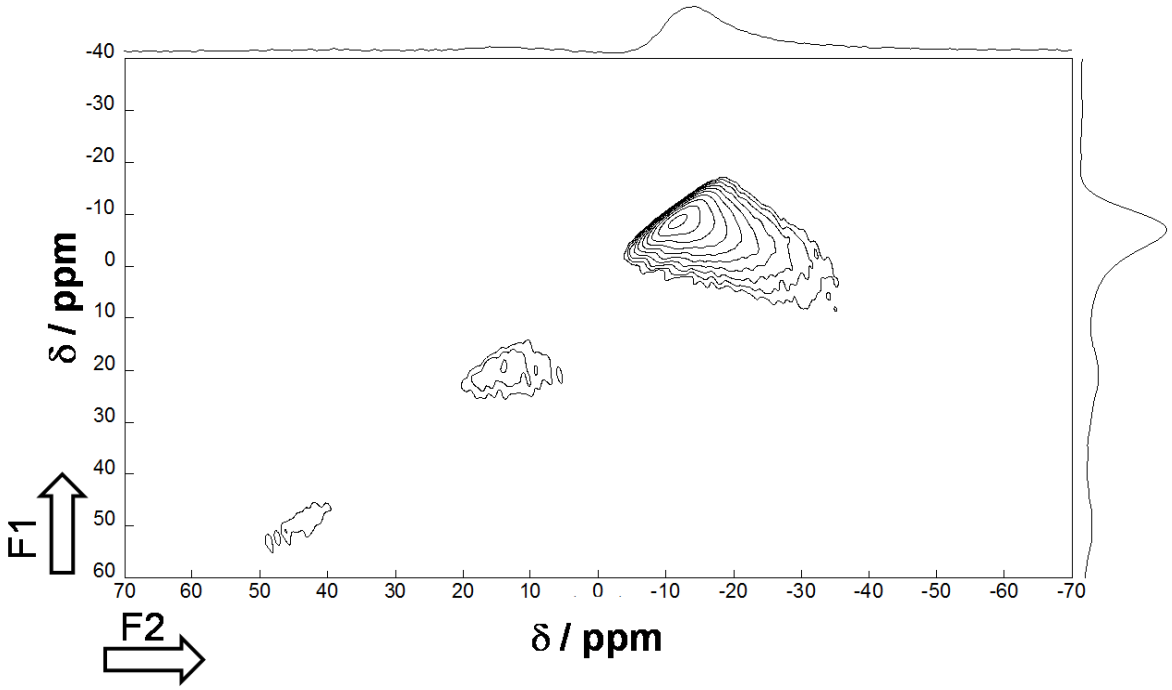

Source:By the Author

A.4. $^{27}Al\{^{31}P\}$-REDOR dephasing curves

Figure 4 - $^{27}Al\{^{31}P\}$ REDOR dephasing curves of glasses in the $[80Ba(PO_3)_2 – 20Al(PO_3)_3]_{100-x}[80BaF_2 – 20AlF_3]_x$ series.

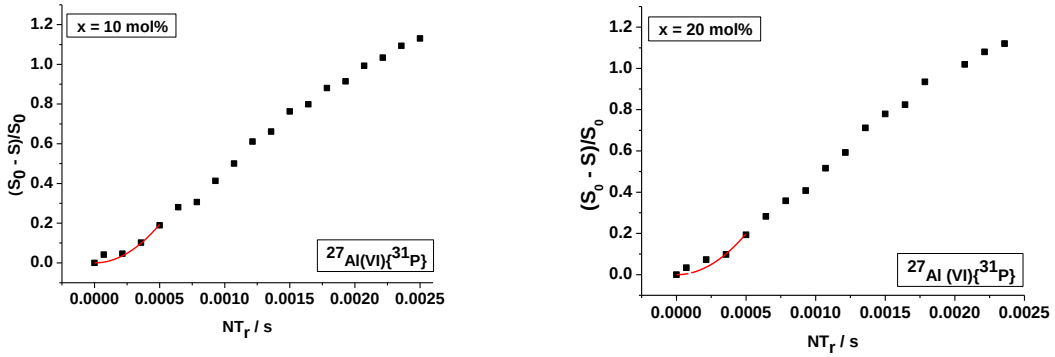

continue

continuation

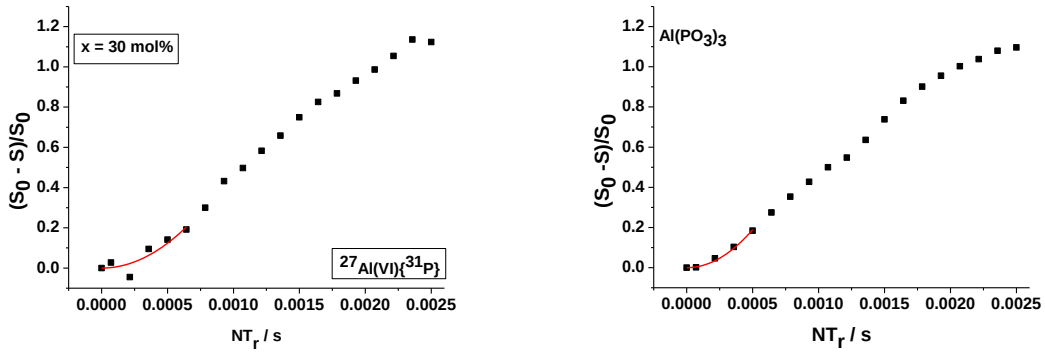

Source:By the Author

A.5. ^{31}P MAS NMR spectra deconvolutions

Figure 5 – ^{31}P MAS NMR spectra with simulations in the $[80Ba(PO_3)_2 – 20Al(PO_3)_3]_{100-x}[80BaF_2 – 20AlF_3]_x$ series at 14.0 kHz.

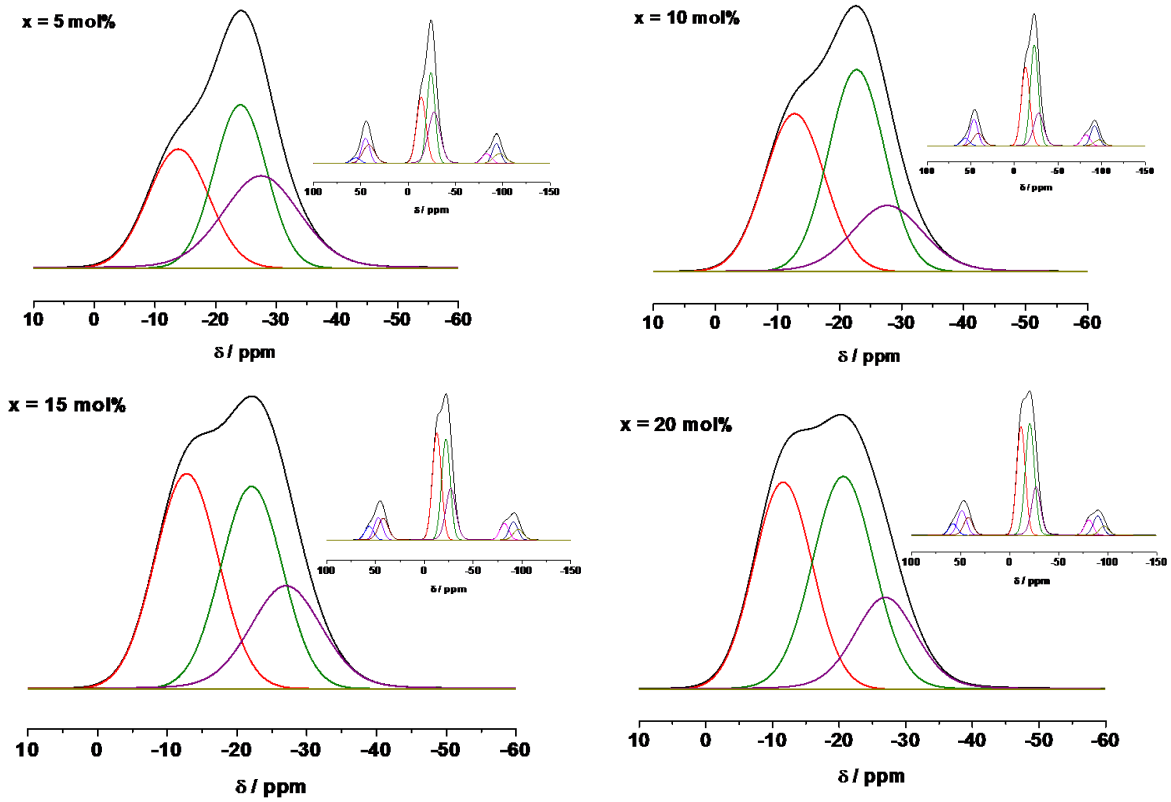

continue

continuation

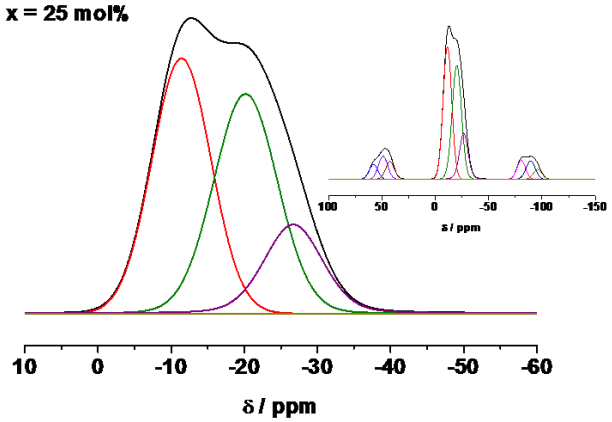

Source:By the Author